Monthly Notices
of the
ROYAL ASTRONOMICAL SOCIETY
MNRAS **467,** 2199–2216 (2017) doi:10.1093/mnras/stx166

The ultracompact nature of the black hole candidate X-ray binary 47 Tuc X9

Arash Bahramian,[1,2]★ Craig O. Heinke,[1] Vlad Tudor,[3] James C. A. Miller-Jones,[3] Slavko Bogdanov,[4] Thomas J. Maccarone,[5] Christian Knigge,[6] Gregory R. Sivakoff,[1] Laura Chomiuk,[2] Jay Strader,[2] Javier A. Garcia[7] and Timothy Kallman[8]

[1]*Department of Physics, CCIS 4-183, University of Alberta, Edmonton, AB T6G 2E1, Canada*
[2]*Department of Physics and Astronomy, Michigan State University, East Lansing 48824, MI, USA*
[3]*International Centre for Radio Astronomy Research – Curtin University, GPO Box U1987, Perth, WA 6845, Australia*
[4]*Columbia Astrophysics Laboratory, Columbia University, New York 10027, NY, USA*
[5]*Department of Physics, Texas Tech University, Lubbock 79409-1051, TX, USA*
[6]*School of Physics and Astronomy, University of Southampton, Southampton SO17 1BJ, UK*
[7]*Harvard–Smithsonian Center for Astrophysics, Cambridge 02138, MA, USA*
[8]*NASA Goddard Space Flight Center, Greenbelt 20771, MD, USA*

Accepted 2017 January 18. Received 2017 January 16; in original form 2016 August 2

ABSTRACT

47 Tuc X9 is a low-mass X-ray binary (LMXB) in the globular cluster 47 Tucanae, and was previously thought to be a cataclysmic variable. However, Miller-Jones et al. recently identified a radio counterpart to X9 (inferring a radio/X-ray luminosity ratio consistent with black hole LMXBs), and suggested that the donor star might be a white dwarf. We report simultaneous observations of X9 performed by *Chandra*, *NuSTAR* and Australia Telescope Compact Array. We find a clear 28.18 ± 0.02-min periodic modulation in the *Chandra* data, which we identify as the orbital period, confirming this system as an ultracompact X-ray binary. Our X-ray spectral fitting provides evidence for photoionized gas having a high oxygen abundance in this system, which indicates a C/O white dwarf donor. We also identify reflection features in the hard X-ray spectrum, making X9 the faintest LMXB to show X-ray reflection. We detect an ∼6.8-d modulation in the X-ray brightness by a factor of 10, in archival *Chandra*, *Swift*and *ROSAT* data. The simultaneous radio/X-ray flux ratio is consistent with either a black hole primary or a neutron star primary, if the neutron star is a transitional millisecond pulsar. Considering the measured orbital period (with other evidence of a white dwarf donor), and the lack of transitional millisecond pulsar features in the X-ray light curve, we suggest that this could be the first ultracompact black hole X-ray binary identified in our Galaxy.

Key words: accretion, accretion discs – stars: Black holes – stars: neutron – globular clusters: individual: 47 Tuc – X-rays: binaries.

1 INTRODUCTION

Low mass X-ray binaries (LMXBs) are systems in which a compact object [neutron star (NS) or black hole (BH)] accretes matter from a low-mass companion (typically a main-sequence star) through Roche lobe overflow or wind-fed accretion (from a red giant). It has been long noticed that the population of LMXBs per unit mass in globular clusters (GCs) is orders of magnitude higher than that of the Galactic field (Katz 1975; Verbunt & Hut 1987; Heinke et al. 2003b; Pooley et al. 2003; Jordán et al. 2004). This overabundance has been associated with the high stellar density in GCs. While most LMXBs in the Galactic field are formed through binary evolution of primordial binaries, it has been shown that in GCs, the dominant channel to form LMXBs is through encounters. These scenarios include tidal capture by an NS or BH, exchange of a compact object into a primordial binary, or collision of a compact object with a red giant (Fabian, Pringle & Rees 1975; Sutantyo 1975; Hills 1976; Bailyn & Grindlay 1990; Davies & Hansen 1998; Ivanova et al. 2006, 2008).

While it is generally understood that NSs are well-represented in GCs, the presence of BHs in GCs is more controversial. Hundreds to thousands of stellar mass BHs form in GCs through stellar evolution. A fraction of these BHs will have sufficient natal kicks to leave the cluster after birth while the rest will sink towards the centre of the cluster and form a dense sub-cluster. It was previously thought the core-collapse of this sub-cluster will result in total evaporation from

★E-mail: bahramian@pa.msu.edu

the GC and thus in most cases no BHs will be left in the cluster (Kulkarni, Hut & McMillan 1993; Sigurdsson & Hernquist 1993). This is consistent with observations of LMXBs in GCs, as all the bright (persistent or transient) LMXBs found in Galactic GCs have been shown to be NS LMXBs (e.g. Verbunt & Lewin 2006; Papitto et al. 2013; Bahramian et al. 2014). For example, the radio/X-ray flux ratio of the transient in NGC 6388 strongly indicates it holds an NS accretor (Bozzo et al. 2011). The NGC 2808 transient is an accreting millisecond X-ray pulsar (Sanna et al. 2017). M15 X-2 produces X-ray bursts, which would not be visible from AC 211 (White & Angelini 2001), but AC 211 also holds an NS, as shown by tomographic analysis (van Zyl et al. 2004).

However, our understanding of the BH LMXB population in GCs has changed significantly over the past few years, with the discovery of highly luminous BH LMXB candidates in extragalactic GCs[1] (e.g. Maccarone et al. 2007; Maccarone & Peacock 2011), as well as quiescent BH LMXB candidates in Galactic GCs (Strader et al. 2012; Chomiuk et al. 2013; Miller-Jones et al. 2015). Additionally, on the theoretical front, recent, more detailed, simulations have found that a substantial fraction of BHs may remain in GCs up to the present day (Morscher et al. 2013, 2015; Sippel & Hurley 2013; Peuten et al. 2016). The recent LIGO detection of a BH–BH merger has also rekindled interest in the formation of such binaries inside GCs (Rodriguez et al. 2015, 2016).

X-ray spectroscopy can help with distinguishing between some types of faint/quiescent X-ray sources in GCs. While cataclysmic variables (CVs) – systems with a white dwarf (WD) accreting from a main-sequence or sub-giant star – tend to show a hard X-ray spectrum dominated by hot bremsstrahlung emission, NS LMXBs (in quiescence) often show a softer spectrum, dominated by blackbody-like emission from the NS surface (Rutledge et al. 1999, 2002; Grindlay et al. 2001; Heinke et al. 2003b).

X-ray spectra of quiescent LMXBs also often show a non-thermal component, fit by a power law with photon index between 1 and 2, which could be produced by continuous low-level accretion (e.g. Campana et al. 1998). While the non-thermal component in quiescent NS LMXBs may be associated either with accretion or with magnetospheric or shock emission related to an active radio pulsar wind (Campana et al. 1998; Jonker, Wijnands & van der Klis 2004; Wijnands et al. 2015), in quiescent BH LMXBs, the X-ray emission is thought to be from a radiatively inefficient accretion flow, possibly synchrotron emission from the jet (Gallo et al. 2007) and/or synchrotron self-Compton emission from the jet base (Plotkin et al. 2015). The non-thermal component has similar properties in NS and BH LMXBs in quiescence, so it can be difficult to distinguish between BH LMXBs and NS LMXBs lacking a strong blackbody-like component. A chief diagnostic method to find BH LMXBs has been based on the ratio of radio and X-ray luminosities of the system during the hard or the quiescent state (Maccarone 2005). BH X-ray binaries (XRBs) show compact partially self-absorbed jet emission in quiescence (and in the hard state during outbursts), making them brighter in radio compared to NS LMXBs with similar X-ray luminosities (Fender, Gallo & Jonker 2003; Gallo, Fender & Pooley 2003; Migliari & Fender 2006).

Millisecond pulsars (MSPs) are old pulsars that have been spun up through accretion from a companion (Alpar et al. 1982). It is thought that NS LMXBs are progenitors of MSPs. Detection of millisecond pulsations in the LMXB SAX J1808.4−3624 (Wijnands & van der Klis 1998) – and later in other LMXBs – clearly demonstrated this scenario. The final evolutionary link connecting LMXBs and MSPs has been found in recent years, in the form of transitional millisecond pulsars (tMSPs), in which the system moves between an accretion-powered state and a rotation-powered one on time-scales as short as weeks (e.g. Archibald et al. 2009; Papitto et al. 2013).

In LMXBs, if the companion is a compact hydrogen-deficient star (e.g. a WD), then the orbital period is short ($P_{\rm orb} < 80$ min), and the system is an ultracompact X-ray binary (UCXB). The depletion of hydrogen in UCXBs leads to high abundances of either helium, if the donor is a low-mass He WD, or carbon and oxygen, if the donor is a more massive C/O WD (Nelemans et al. 2004). In the case of UCXBs with C/O WDs, the overabundance of carbon and oxygen can produce observable diagnostics in far-ultraviolet (FUV) and X-ray spectra (Nelemans et al. 2010).

47 Tucanae (47 Tuc) is a dense, massive ($6.5 \times 10^5\,{\rm M}_\odot$; Kimmig et al. 2015) Galactic GC at a distance of 4.53 kpc[2] (Woodley et al. 2012; Bogdanov et al. 2016). Low extinction [$E(B-V) = 0.04$; Salaris et al. 2007) makes this cluster easy to study. 47 Tuc harbours ∼230 X-ray sources with $L_{\rm X} \gtrsim 10^{29}$ erg s^{-1} (Heinke et al. 2005b), including 23 radio MSPs (Freire et al. 2003; Pan et al. 2016), and many CVs and chromospherically active binaries (Grindlay et al. 2001; Knigge et al. 2002, 2003, 2008; Edmonds et al. 2003a,b). As the cluster has a very high stellar encounter rate (Bahramian et al. 2013), it should produce many XRBs. Indeed, five quiescent NS LMXBs, all with prominent thermal blackbody-like components in their X-ray spectra (two also have strong non-thermal components), have been identified and studied in 47 Tuc (Heinke et al. 2003a, 2006; Heinke, Grindlay & Edmonds 2005a; Bogdanov et al. 2016).

X-ray emission from 47 Tuc was first noticed in observations by *Einstein*, and the source was identified as 1E 0021.8−7221 (Hertz & Grindlay 1983; Grindlay et al. 1984). In *HST* observations, a variable blue star – named V1 – was discovered and identified as a likely CV and the counterpart of 1E 0021.8−7221, by Paresce, de Marchi & Ferraro (1992). The relatively high X-ray luminosity, low optical/X-ray ratio, and hints of a 120-s periodicity in *Einstein* data (Auriere, Koch-Miramond & Ortolani 1989), inspired the suggestion that V1 (1E 0021.8−7221) was an intermediate polar, where the modulation would be due to rotation of the WD (Paresce et al. 1992). Later, *ROSAT* observations found nine X-ray sources within the cluster, and identified X9 as the counterpart for 1E 0021.8−7221 (Verbunt & Hasinger 1998, who argued, presciently, that X9 was likely an LMXB). The association of V1 and X9 was later confirmed by *Chandra* observations (Grindlay et al. 2001). X9 showed rapid (∼hours) X-ray and optical/UV variability, with a hint of a ∼6-h periodicity in the UV flux (Paresce et al. 1992). Time series analysis of *V* and *I* light curves by Edmonds et al. (2003b) indicated a marginal 3.5-h (or 7 h, if due to ellipsoidal variations) periodicity. *HST* FUV spectroscopy of X9 showed strong, double-peaked C IV emission lines, confirming the presence of an accretion disc and/or disc wind in the system (Knigge et al. 2008).

X9 is the brightest ($\gtrsim 10^{33}$ erg s^{-1}) X-ray source in the core of 47 Tuc with a hard spectrum (Grindlay et al. 2001; Heinke et al. 2005b). In both *Einstein* and *ROSAT* observations, X9 has shown clear variability. The first *Chandra* study of X9 (aka W42, as designated by Grindlay et al. 2001) in 2000 suggested the

[1] Discovery of NS ultraluminous X-ray sources in recent years (Bachetti et al. 2014; Furst et al. 2016; Israel et al. 2016, 2017) indicate that X-ray luminosity $\gtrsim 10^{39}$ erg s^{-1} in a single object does not guarantee a BH accretor.

[2] This value is derived from a compilation of 22 distance measurements, as reported by Bogdanov et al. (2016).

presence of a 218-s modulation in the light curve, which, if verified, would mark X9 as an intermediate polar CV (Grindlay et al. 2001). Spectral analyses of the *Chandra* X-ray data showed a complex spectrum with a very hard non-thermal component and extremely strong oxygen spectral lines (Heinke et al. 2005b).

Recently, Miller-Jones et al. (2015) reported on deep radio observations of 47 Tuc, in which they detected a radio counterpart for X9. They reported that the ratio of radio/X-ray luminosity for X9 is strongly inconsistent with a CV, and more consistent with a BH LMXB, or possibly a tMSP (deemed unlikely from the X-ray spectral and variability properties). Based on the brightness (and thus accretion rate) and evidence against strong Hα emission from *HST* narrow-band photometry, they suggested the system might be a UCXB. They further inferred an orbital period of ∼25 min, from a correlation between quiescent X-ray luminosity and time-averaged mass-transfer rate from the companion, and using calculations of the time-averaged mass-transfer rate at different orbital periods in UCXBs. Note that, this was not based on detection of a periodic signal.

In this work, we study the X-ray properties of X9, as observed by *Chandra* and *NuSTAR*, and the radio/X-ray flux ratio from simultaneous radio observations. We describe the data used in this work, along with a description of reduction and analysis methods, in Section 2. In Section 3, we present results and in Section 4, we will discuss the implications of these findings.

2 DATA AND ANALYSIS

We obtained simultaneous radio and X-ray observations of X9 with the Australia Telescope Compact Array (ATCA), *Chandra* using the ACIS-S detector, and *NuSTAR*, on 2015 February 02 (MJD = 57055; ATCA from 05:00 to 17:00 UT on February 02, *Chandra* from 14:25 on February 02 to 03:20 on February 03, and *NuSTAR* from 11:51 on February 02 to 00:46 on February 05, all UT). We also analysed *Chandra* observations from late 2014 (described in Bogdanov et al. 2016) and archival *Chandra*/ACIS, *Chandra*/HRC, *Swift*/XRT, *ROSAT*/HRI(High Resolution Imager) and *Einstein* data to study the variability of X9 over long time-scales (∼ days to years).

2.1 *Chandra*/ACIS

Archival *Chandra*/ACIS data were obtained in 2000 (with ACIS-I3) and 2002 (with ACIS-S3) in faint mode. Our 2014–15 campaign (PI: Bogdanov) included six observations between 2014 September 2014 and 2015 February (Table 1). All observations in this campaign were performed in very faint mode on ACIS-S3. We focus our spectral analysis upon the 2015 *Chandra* observation; detailed analysis of other archival *Chandra* spectra is deferred to future papers.

We used CIAO 4.7 with CALDB 4.6.8 (Fruscione et al. 2006) for data reprocessing and analysis. We reprocessed all *Chandra* data with CHANDRA_REPRO and extracted source and background spectra using SPECEXTRACT. We chose an extraction radius of 1.8 arcsec for the source region. For light-curve analysis, we barycentered the time stamps. 47 Tuc X9 is near the crowded centre of the cluster. Thus, for extracting background spectra, we used an annulus with inner and outer radii of 2.7 and 7.4 arcsec around the source, excluding detected sources (Fig. 1). Depending on exposure and data quality, we binned all final spectra to either 50 or 20 counts per bin. Finally we used XSPEC 12.8.2 (Arnaud 1996) for

Table 1. The X-ray data used in this study. *Einstein*/HRI and *ROSAT* data were obtained from Auriere et al. (1989) and Verbunt & Hasinger (1998), respectively. All *Chandra*, *NuSTAR* and *Swift*/XRT were reduced and analysed in this study.

Observatory/Inst.	Obs. ID	Date	Exposure (ks)
Einstein/HRI	658	1979-04-21	1.6
	4858	1979-11-18	0.8
	4857	1979-11-19	1.5
	4855	1979-11-19	2.0
	4856	1979-11-19	1.9
Einstein/IPC	4969A	1979-11-19	4.8
	4969B	1979-11-20	4.8
	4969C	1979-11-21	7.2
ROSAT/HRI	300059N00	1992-04-19	1.2
	300059N00	1992-05-21	3.4
	300059A01	1993-04-17	13.2
	400738N00	1994-11-30	18.9
	400809N00	1995-10-25	4.6
	400809A01	1996-11-16	17.5
Chandra/ACIS	00953	2000-03-16	32
	00955	2000-03-16	32
	02735	2002-09-29	65
	02736	2002-09-30	65
	02737	2002-10-02	65
	02738	2002-10-11	69
	16527	2014-09-05	41
	15747	2014-09-09	50
	16529	2014-09-21	25
	17420	2014-09-30	09
	15748	2014-10-02	16
	16528	2015-02-02	40
Chandra/HRC	5542	2005-12-19	50
	5543	2005-12-20	51
	5544	2005-12-21	50
	5545	2005-12-23	52
	5546	2005-12-27	48
	6230	2005-12-28	45
	6231	2005-12-29	47
	6232	2005-12-31	44
	6233	2006-01-02	97
	6235	2006-01-04	50
	6236	2006-01-05	52
	6237	2005-12-24	50
	6238	2005-12-25	48
	6239	2006-01-06	50
	6240	2006-01-08	49
Swift/XRT	84119001	2014-11-04	1.8
	84119002	2014-11-17	4.2
	84119003	2014-11-29	4.0
	84119004	2014-12-11	4.2
	84119005	2014-12-23	3.9
	84119006	2015-01-07	3.7
	84119007	2015-01-16	3.1
	84119008	2015-01-28	3.3
	84119009	2015-02-09	4.1
	84119010	2015-03-05	3.8
	84119011	2015-03-17	4.0
	84119012	2015-03-29	3.9
	84119013	2015-04-10	3.8
	84119014	2015-04-22	3.6
NuSTAR	80001084002	2015-02-02	17
	80001084004	2015-02-03	76

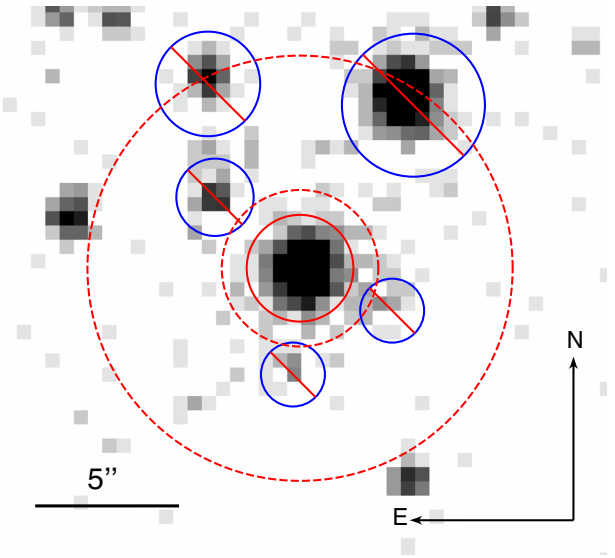

Figure 1. *Chandra* 0.3–10-keV image of the vicinity of X9 in the core of 47 Tuc. Circles represent the nominal source (solid-lined red circle) and background (dashed red circle) regions for spectral extractions of 47 Tuc X9. X-ray sources present in the background were excluded from the extraction region (blue circles).

spectral analysis, and performed spectral fitting in the 0.4–10-keV band.

2.2 *NuSTAR*

NuSTAR has a relatively large point-spread function, with a half-power diameter of ∼1 arcmin (Harrison et al. 2013), which encloses a substantial fraction of the core of 47 Tuc (Fig. 2, left-hand panel). 47 Tuc X9 is easily the brightest X-ray source above 2 keV within the half-mass radius of 47 Tuc (Heinke et al. 2005b). The CV AKO 9 (Knigge et al. 2003) is the only other source detected above 6 keV in our simultaneous *Chandra* observation. However, AKO 9 is ∼20 times fainter than X9 in the 6–10-keV band (Fig. 2, middle and right-hand panels). This makes X9 the principal source of X-rays above 6.0 keV in the cluster and ensures that *NuSTAR* spectra above 6 keV are minimally affected by confusion. We also checked the coordinates of the detected source, and find it consistent with the reported coordinates of X9.

Our *NuSTAR* observation of 47 Tuc was performed between 2015 February 02 and 05 and was simultaneous with *Chandra* ObsID 16528 and with our ATCA radio observation. Our *NuSTAR* observation was performed in two segments with a gap from February 02, 21:11, to 03, 08:46 UT (Table 1).

X9 is clearly detected in our *NuSTAR* observations (Fig. 2, left-hand panel). The suggested extraction radius for weak sources in *NuSTAR* data is 30 arcsec (*NuSTAR* observatory guide). We used this radius for all our spectral extractions (source and background). We used the 6–79-keV band for all *NuSTAR* data analysis of X9.

We used the NUSTARDAS package released with HEASOFT 16.6 for data reprocessing and analysis. We processed the observations by running NUPIPELINE and proceeded to extract spectra and light curves from both modules (FPMA and FPMB) using NUPRODUCTS. After grouping the spectra by counts (20 per bin for the shorter segment and 40 for the longer segment), we used XSPEC for spectral analysis.

2.3 *Chandra*/HRC

The 47 Tuc *Chandra*/HRC campaign (PI: Rutledge; Cameron et al. 2007) contains 15 × 50-ks observations performed over a period of 20 d in 2005 December and 2006 January (Table 1). This provided us with a unique opportunity to study variations of X9 on time-scales of days. We combined these observations using `reproject_obs` and extracted X9's light curve running `dmextract` (in CIAO software package) with background subtraction and assuming Gehrels uncertainties (Gehrels 1986). Finally, we barycentered the time stamps, and binned the light curve (if needed) into intervals of 10 ks, or 10 s (for different periodicity searches).

2.4 *Swift*/XRT, *ROSAT*/HRI and *Einstein*

As X9 shows strong variability in X-rays, we also investigated available archival data from *Swift*/XRT, *ROSAT*/HRIand *Einstein* to study the extent of these variations.

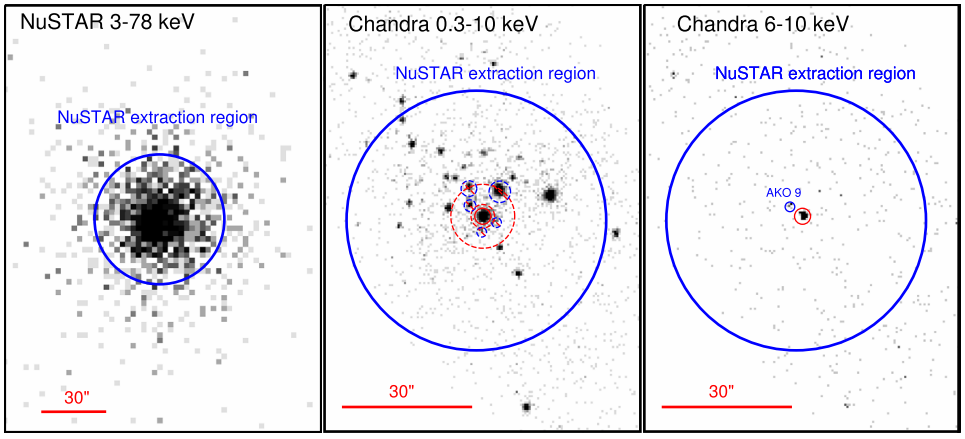

Figure 2. X-ray image of X9 in 47 Tuc as observed by *NuSTAR* (left-hand panel) and *Chandra*/ACIS (centre and right-hand panels). X9 is the only significant source above 6 keV in *Chandra* observations and thus is the major contributor in *NuSTAR* data of the cluster. The solid-lined blue circle represents our spectral extraction region for X9 in *NuSTAR* data.

Since 2014, *Swift* has observed 47 Tuc frequently with long (∼4000 s) exposures as part of a GC monitoring programme[3] (Linares & Chenevez, inpreparation). Unlike typical *Swift*/XRT exposures (∼1000–2000 s), these exposures are adequate to constrain the brightness of sources at a few $\times 10^{33}$ erg s^{-1} at a distance of 4.5 kpc (like X9). Thus, we analyse these data sets to look for variability and possible brightening (e.g. due to enhanced accretion) from X9.

However, due to the relatively low resolution and large point-spread function of (FWHM ∼7 arcsec; Burrows et al. 2005), the X-ray sources in 47 Tuc blend together in these observations. We chose to extract events in the 4–10-keV band, in which X9 is the dominant source, as a trade-off between signal/noise ratio and dominance of X9's flux over the rest of the cluster. After measuring background-subtracted count rates in the 4–10-keV band for each observation and subtracting contamination from other cluster sources in the *Swift*/XRT extraction region (based on their flux in the 4–10-keV band *Chandra* image), we converted these count rates to flux by folding the best-fitting spectral model found for our 2015 *Chandra*/ACIS + *NuSTAR* spectrum (see Section 3.2) through the *Swift*/XRT response matrix (using XSPEC) and finding equivalent flux values for each measured count rate. Ultimately, we converted flux values to luminosity in the 0.5–10-keV band, assuming a distance of 4.53 kpc to 47 Tuc.

There are also archival *ROSAT*/HRI data available for 47 Tuc taken between 1991 and 1997 (0.5–2.5 keV), with spatial resolution (∼2 arcsec) capable of marginally resolving the core of 47 Tuc (with radius of ∼21.6 arcsec). Detailed analyses of these data, attributing counts to each of the brightest core sources, have been reported by Verbunt & Hasinger (1998). Thus, we use the count rates reported by them (Verbunt & Hasinger 1998, fig. 3) in our analysis. Similar to our procedure for *Swift* data, we used the best-fitting spectral model folded to *ROSAT*/HRI to convert count rates to flux and luminosity.

Among the instruments on board *Einstein*, the HRI was sensitive in the 0.15–3.0-keV band with a spatial resolution of ∼2 arcsec, and the Imaging Proportional Counter (IPC) was sensitive in the 0.4–4.0-keV band with a resolution of ∼1 arcmin. Although HRI had excellent spatial resolution, it had a low effective area (5–20 cm^2). In contrast, IPC had a relatively large effective area (100 cm^2). *Einstein* observed 47 Tuc eight times in 1979 (five HRI observations followed with three IPC observations) and 1E 0021.8−7221 was clearly detected in all observations (Hertz & Grindlay 1983; Auriere et al. 1989). We use the reported fluxes from Auriere et al. (1989) in our analysis.

Although *ROSAT*/HRI and *Einstein* have relatively poor angular resolutions, the high luminosity of X9 and its particularly hard spectrum compared to other sources in 47 Tuc's core allows us to use these observations to study X9.

All *Swift*/XRT, *ROSAT* and *Einstein* observations used in this study are listed in Table 1.

2.5 ATCA

Since the existing radio and X-ray data on 47 Tuc X9 were taken several years apart (Miller-Jones et al. 2015), we requested additional ATCA data to be simultaneous with the scheduled *Chandra* observations in 2015 February, under project code C3012. The ATCA data were taken from 0505–1705 UT on 2015 February 2, with the array in an extended 6-km configuration. Using the Compact Array Broadband Backend (Wilson et al. 2011), we observed simultaneously in two frequency bands, each of bandwidth 2048 MHz, centred at 5.5 and 9.0 GHz. 90 min of data were lost to bad weather, leaving us a total of 523 min on source.

We used B1934−638 both to set the amplitude scale and to determine the instrumental frequency response. The starting elevation of the target was 52°, which decreased with time. For the first 10 h of observations, we were able to use the same nearby compact source, B2353−686, to determine the time-variable complex gains as used by Miller-Jones et al. (2015). However, that source set below the elevation limit of the telescope at 1445 UT, after which we switched to the more distant, but higher elevation complex gain calibrator J0047−7530 to enable continued observations of 47 Tuc. We reduced the data according to standard procedures within the Multichannel Image Reconstruction, Image Analysis and Display (MIRIAD) software package (Sault, Teuben & Wright 1995), and then exported the calibrated, frequency-averaged data to the Common Astronomy Software Application (CASA; McMullin et al. 2007) for imaging. We co-added all the data and used a Briggs robust weighting of 1 to produce the image. We detected X9 in both frequency bands and used the CASA task IMFIT to fit a point source to the target in the image plane. This gave measured flux densities of 27.6 ± 7.2 and 30.7 ± 8.9 μJy bm^{-1} at 5.5 and 9.0 GHz, respectively, giving a measured spectral index (defined such that flux density S_ν scales with frequency ν as $S_\nu \propto \nu^\alpha$) of $\alpha = 0.2 \pm 0.8$.

Comparing with observations in 2010 and 2013 (Miller-Jones et al. 2015), the 9-GHz radio emission is similar, although the 5.5-GHz emission has dropped by a factor of 1.5 ± 0.4.

3 RESULTS

3.1 X-ray variability

Einstein observations of 47 Tuc in the 1980s indicated that 1E 0021.8−7221 (the only detected X-ray source in the cluster at the time) showed strong variations. Auriere et al. (1989) reported a variable absorbed flux of 2.2–6.4 $\times$ 10^{-12} erg cm^{-2} s^{-1} in the 0.4–2.0-keV band. Assuming a distance of 4.53 kpc and extrapolating these luminosities to the 0.5–10-keV band using the power-law model reported by Auriere et al. (1989), with a photon index of 2, we find a luminosity range of 6.3–21.5 $\times$ 10^{33} erg s^{-1} for *Einstein*/HRI and *Einstein*/IPC data points.

In *ROSAT*/HRI observations of 47 Tuc between 1992 and 1996 (Verbunt & Hasinger 1998), X9 showed a variable brightness between 1.5 and 6.1 $\times$ 10^{33} erg s^{-1} (extrapolated to the 0.5–10-keV band). Similar variations can be seen in *Chandra*/ACIS campaigns in 2000, 2002 and 2014–2015, and recent deep *Swift*/XRT observations of the cluster (Fig. 3).

3.1.1 Superorbital modulation

The *Chandra*/HRC light curve of X9 shows strong modulations between 1.1 $\times$ 10^{33} erg s^{-1} and 8.4 $\times$ 10^{33} erg s^{-1} on time-scales of a few days (Fig. 3). We used a generalized Lomb–Scargle periodogram algorithm[4] (Lomb 1976; Scargle 1982) implemented in the

[3] http://www.iac.es/proyecto/SwiftGloClu/

[4] Compared to the 'standard' Lomb–Scargle periodogram, the 'generalized' one utilized here allows for a constant offset term in the model and it also incorporates data uncertainties (e.g. see Zechmeister & Kürster 2009; Vanderplas et al. 2012).

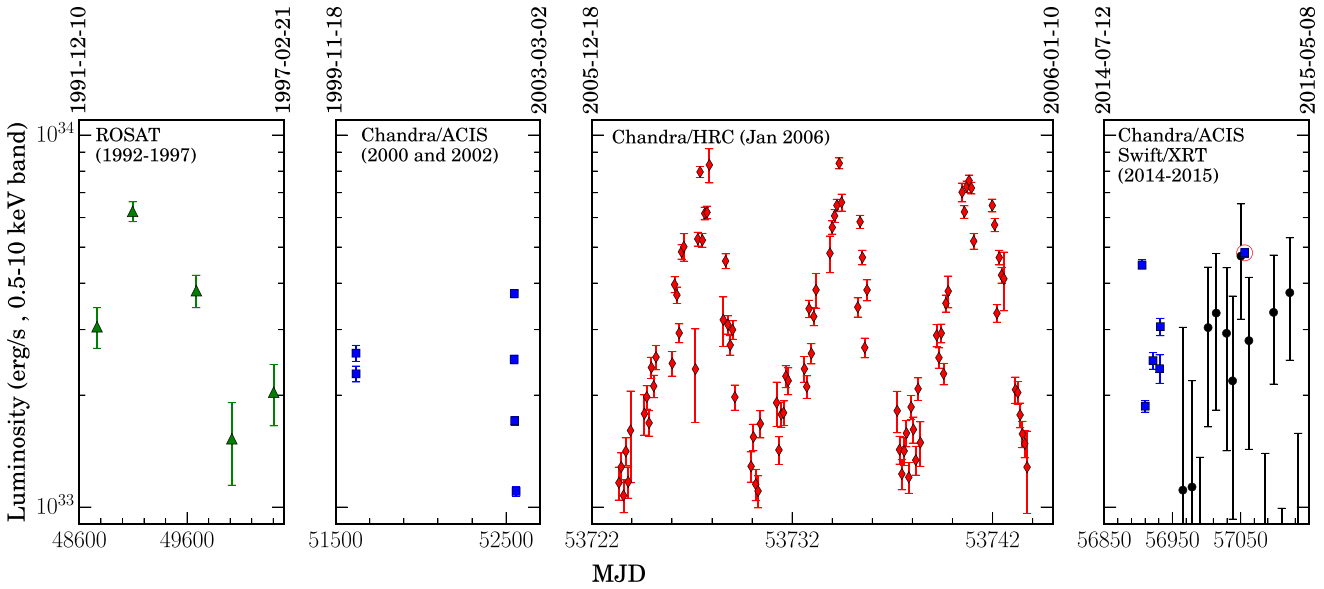

Figure 3. Light curve of 47 Tuc X9 as seen by various telescopes since 1991. Note that, each panel has a different time-scale. Green triangles show *ROSAT*/HRI observations performed in the 1990s (Verbunt & Hasinger 1998), blue squares represent *Chandra*/ACIS campaigns in 2000 (Grindlay et al. 2001), 2002 (Heinke et al. 2005b) and 2014–2015 (Bogdanov et al. 2016; this work). Red diamonds show *Chandra*/HRC observations between 2005 December and 2006 January (Cameron et al. 2007) and black circles show *Swift*/XRT observations (Linares & Chenevez, inpreparation). The *Chandra*/ACIS observation performed simultaneously with *NuSTAR* and ATCA is indicated with a red circle around the blue square.

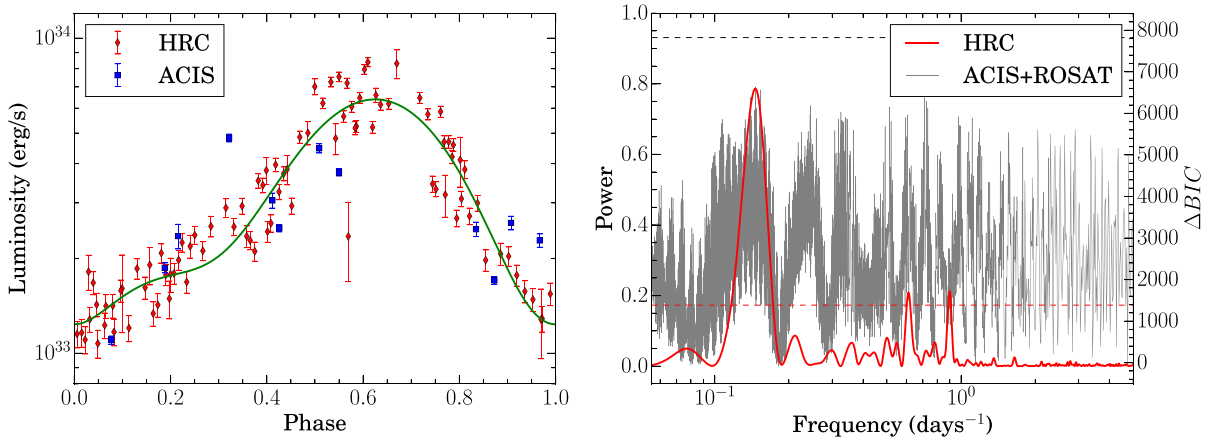

Figure 4. Left-hand panel: folded X-ray light curve of X9 and a second-order Fourier fit with a period of 6.8 d for HRC and ACIS data. The folded light curve of X9 shows non-sinusoidal behaviour with a slower rise and a faster drop. Right-hand panel: result of a periodicity search using the Lomb–Scargle method for HRC data (red line) and for *Chandra*/ACIS + *ROSAT*/HRI data (grey line). The red and grey dashed horizontal lines indicate the 95 per cent confidence thresholds calculated using bootstrap resampling. Note that the uncertainties found with this method might be overestimated due to the non-sinusoidal profile of oscillations.

PYTHON package ASTROML[5] (Vanderplas et al. 2012; Ivezić et al. 2014) to constrain the period of the variability observed in *Chandra*/HRC data. We detected a formally significant periodic signal with a period of $6.8^{+1.8}_{-1.0}$ d for HRC data (Fig. 4, right-hand panel; red line).

Given the limited number of cycles observed in the light curve (∼ three), we test if it is possible for the apparent periodicity to be a false detection, caused by red noise (e.g. Vaughan et al. 2016). Thus, we check this possibility, by generating a large sample of red-noise light curves following Timmer & Koenig (1995). We used the package DELIGHTCURVESIMULATION[6] (Connolly 2015) to generate 50 000 red-noise light curves with a broken power-law power spectrum, with conservative power-law indices of 1.1 and 2.2 (e.g. see Reig, Papadakis & Kylafis 2003), placing the break at our detected period (as the most conservative case). We find that the probability of achieving a significant periodicity due to red noise with a power similar to (or higher than) that seen in our data is 0.07 per cent. Thus, we conclude that the signal appears likely to be periodic, or quasi-periodic.

[5] http://www.astroml.org/

[6] https://github.com/samconnolly/DELightcurveSimulation

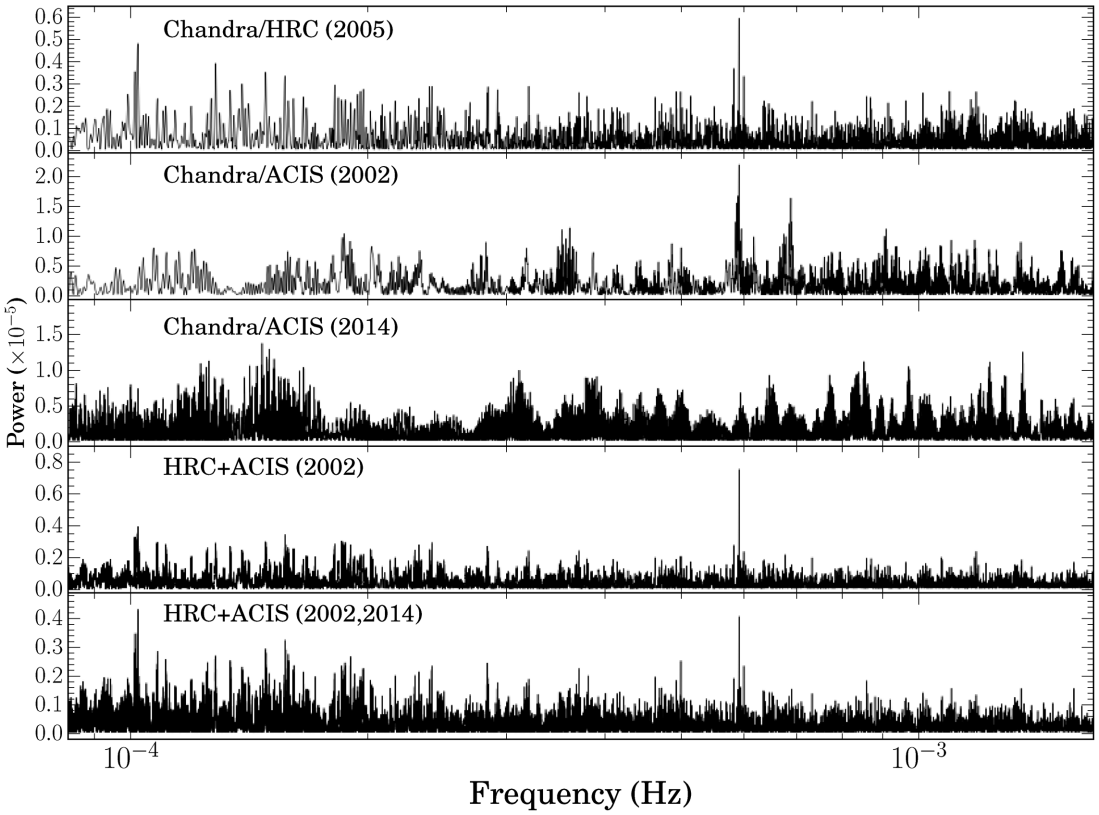

Figure 5. *Chandra* power spectra for a periodicity search in the 10 min to 4 h range. A significant peak ($>5\sigma$) is visible at 5.9×10^{-4} Hz (28.2 min) in the *Chandra*/HRC and *Chandra*/ACIS 2002 light curves. Such a signal is not clearly detected in the *Chandra*/ACIS 2014 light curve. The two bottom panels show the power spectra computed for combined light curves.

The uncertainties reported for the period here are calculated based on bootstrap resampling. A second-order Fourier fit describes the light curve significantly better than a first-order fit, with an F-test probability of chance improvement of 7×10^{-11} per cent for HRC data.[7] The two-term Fourier fit shows the rise towards the peak is slower than the fall (Fig. 4, left-hand panel).

The periodicity is only clearly visible in the *Chandra*/HRC data. However, we also searched for indications of this variability in the *ROSAT*/HRI and *Chandra*/ACIS data. We performed a period search using the Lomb–Scargle method with *ROSAT*/HRI and *Chandra*/ACIS data points, excluding the *Chandra*/HRC light curve. This search provides no clear periodic signal, but the maximum power in this periodogram is located at $P = 6.8$ d (Fig. 4, right-hand panel). Although such a peak is insignificant by itself, given the consistency with the signal detected in *Chandra*/HRC data, it adds suggestive evidence that the signal is real.

The statistical significance of this 6.8-d periodicity in the *Chandra*/HRC data is strong enough that it is likely to be real, but this result is not conclusive. The strong suggestion of a similar periodicity at different times in *Chandra*/ACIS and *ROSAT*/HRI data adds to the likelihood that the periodicity is real. We note the inherent problems in definitively identifying periods against red-noise backgrounds with small numbers of cycles (Press 1978; Vaughan et al. 2016), and we believe some caution is warranted in taking this signal as strong evidence of a periodicity. We consider the possible implications of such a periodicity, if confirmed, below (Section 4.3). This period cannot be orbital, since the optical/IR counterpart is far too dim to allow a (sub-giant) donor that would be needed to fill the Roche lobe with such an orbit (Knigge et al. 2008; Miller-Jones et al. 2015).

[7] An F-test for the third-order Fourier term provides a probability of 4.5 per cent for obtaining such improvement by chance; thus, we prefer the two-term model.

3.1.2 *Orbital periodicity*

The long exposures of the *Chandra*/HRC campaigns in 2005 enabled us to search effectively for signatures of periodic variability on short time-scales (milliseconds to hours). We used a Lomb–Scargle periodogram to look for signs of an orbital period in the physically motivated range of 10 min to 4 h (where the upper limit is set by the constraints on the donor from the UV/optical photometry; Knigge et al. 2008). We detect a strong signal at 28.18 ± 0.02 min (Fig. 5, top panel). This motivated a search for similar signals in the *Chandra*/ACIS light curves. We find a similarly strong signal in the 2002 *Chandra*/ACIS 0.3–10-keV light curve (Fig. 5, second panel from top). However, this signal is not clearly detected in the 2014 *Chandra*/ACIS light curve (Fig. 5, middle panel).

To ensure the detected signals in the *Chandra*/HRC and *Chandra*/ACIS (2002) light curves are not coincidentally matched noise peaks, we computed the power spectrum for the combined light curve. This significantly increased the significance of the signal (to higher than 5σ), indicating that this signal is coherent, and real (Fig. 5, second panel from the bottom). This detected periodic signal is in remarkable agreement with the predicted orbital period

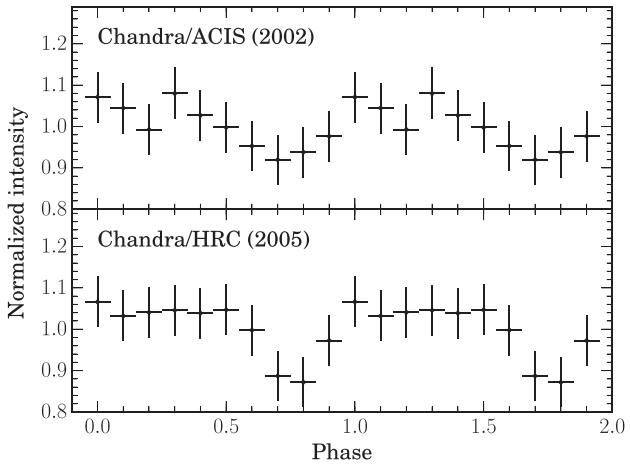

Figure 6. *Chandra*/ACIS (2002) and *Chandra*/HRC light curves folded to a period of 28.2 min (1690.7738 s).

of ∼25 min by Miller-Jones et al. (2015), and supports the UCXB nature of this system.

To determine the significance of the detected signal in the combined light curve, we simulated a large sample (3.5×10^6) of white noise light curves based on our data and measured the peak amplitude in the power spectra. We neglect effects of red noise in these simulations, due to the large sampling baseline and the flat power spectrum in the physically motivated range (10 min to 4 h). None of our simulated light curves show a peak amplitude similar to or higher than our actual data. Thus, we infer a significance of higher than one in 3.5×10^6, or higher than 5σ.

The *Chandra*/HRC and 2002 *Chandra*/ACIS light curves, folded at the peak value of the period, are shown in Fig. 6. Both show evidence for a similar dip, lasting ∼30 per cent of the orbit, and reducing the flux by ∼15 per cent.

We computed power spectra for the *Chandra*/ACIS 2002 light curve in different energy bands (0.3–0.5, 0.5–0.7, 0.7–1.5 and 1.5–7 keV) to determine the spectral component responsible for the periodic variations. We find that the periodic signal is strongly present (but not exclusively) in the 0.5–0.7-keV band (Fig. 7), where the dominant spectral features are two oxygen (VII and VIII) lines in the system. We discuss spectral analysis of the system and these lines in detail in Section 3.2. However, to identify the nature of the change in the spectrum causing the modulation, we extract spectra from the 'high' and 'low' phases as seen in the folded light curve (Fig. 6). We find that the most significant difference between the two phases is the relative strength of the oxygen lines.

The absence of the periodic signal in the *Chandra*/ACIS 2014/2015 campaign could be due to the reduced sensitivity of the *Chandra*/ACIS detector (Marshall et al. 2004). Between 2002 and 2014, the ACIS-S sensitivity below 1 keV dropped by a factor of ∼3 (see *Chandra* threads, ACIS QE Contamination).[8] Given that the amplitude of the variation is ∼15 per cent and is dominantly below 1 keV, a drop by a factor of 3 in sensitivity is sufficient to weaken the signal. The shorter exposure of the 2014/2015 campaign (181 ks, compared to 264 ks in 2002 and 783 ks in 2005) could contribute as well.

[8] http://cxc.harvard.edu/ciao/why/acisqecontam.html

3.1.3 Search for other short-term variability

We also searched for other short-time-scale (milliseconds–minutes) pulsations/modulations in the barycentred HRC data. Looking for second/minute periodic variability (e.g. the previously suggested 218-s modulation; Grindlay et al. 2001), we found no evidence of such modulations.

Since X9 is in a compact binary, the rapid motion of a putative MSP in its orbit would spread the pulsed signal power over numerous Fourier bins in the power spectrum, which greatly diminishes its detectability. Moreover, due to the relatively low X-ray source count rate, it is not possible to search for millisecond pulsations over short segments of the orbit to minimize this effect. Therefore, to search for fast pulsations, we considered two Fourier-domain techniques from the PRESTO software suite (Ransom, Eikenberry & Middleditch 2002; Ransom, Cordes & Eikenberry 2003). The 'acceleration search' technique attempts to compensate for the large spin period derivative induced by the fast orbital motion of the pulsar. This method is most effective when the duration of the observation is $\lesssim$25 per cent of the orbital period. The 'sideband' (phase modulation) method, on the other hand, looks for sidebands produced by the binary motion in the power spectrum centred around the candidate pulsar spin frequency and co-adds them in order to recover some sensitivity to the pulsed signal. This technique is most sensitive in situations where the observation is much longer than the orbital period and the observation is uninterrupted (Ransom et al. 2003). Given that the *Chandra* HRC exposures are tens of kiloseconds, much longer than the apparent orbital period of X9, the phase-modulation method is more appropriate for this source.

For these searches, it is necessary to bin the event data, which causes frequency-dependent attenuation of the periodic signal, with decreased sensitivity at high frequencies (see, e.g., Middleditch 1976; Leahy et al. 1983). We searched each *Chandra* HRC exposure separately, since the observations are too far apart to search them coherently for millisecond pulsations using these methods. We found no statistically significant signal down to 1 ms (aside from the aliases of the 16-μs time sampling). To derive a pulsed fraction upper limit, we used tools available in PRESTO that consider the maximum power found in the power spectrum (see Vaughan et al. 1994, for details). Based on the non-detection in the longest observation, we derive a 90 per cent confidence upper limit of 19 per cent on the pulsed fraction.

3.1.4 Enhanced brightness in 1979

One *ROSAT*/HRI observation of 47 Tuc in 1993 shows X9 at a luminosity of $6.1 \pm 0.4 \times 10^{33}$ erg s^{-1}, which, in comparison with later *ROSAT*/HRI and *Chandra*/ACIS observations, was thought to be caused by an enhanced activity like a flare or outburst (Verbunt & Hasinger 1998). However, the *Chandra*/HRC data shows that X9 reaches a peak luminosity of $\sim 7 \pm 0.2 \times 10^{33}$ erg s^{-1} periodically, and thus this level of brightness for X9 is not unusual.

However, the peak luminosities observed by *Chandra*/HRC or *ROSAT*/HRI are ∼3.5 times fainter than the peak luminosity observed by *Einstein* HRI observations in 1979 ($\sim 2.15 \times 10^{34}$ erg s^{-1} extrapolated to the 0.5–10-keV band). We note that due to the poor spatial resolution of *Einstein*/IPC (3 arcmin), the IPC data analysed by Auriere et al. (1989) contains the entire half-mass radius of the cluster and may be the sum of flux from multiple sources. However, the peak of the light curve was recorded by the *Einstein*/HRI, which has superior spatial resolution (∼2 arcsec), and localized the brightest *Einstein* source to only 1.4 arcsec away from X9.

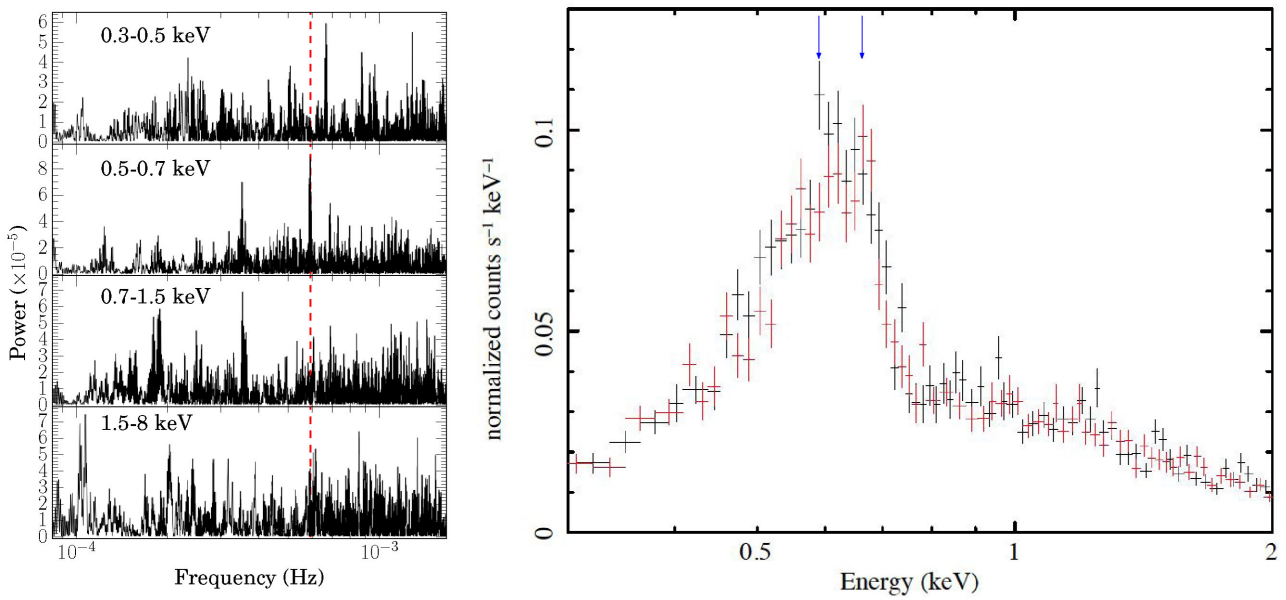

Figure 7. Left-hand panel: power spectrum computed from the *Chandra*/ACIS 2002 light curve in different bands. The vertical red dashed line indicates the location of the detected peak in the full-band light curves. A peak is clearly visible in the 0.5–0.7-keV band. However, there is a weaker signal in the 1.5–8.0-keV band, indicating the signal is not exclusively present in one band. Right-hand panel: *Chandra*/ACIS spectrum of X9 in the 'high' and 'low' phases. The chief difference appears in the oxygen lines (O VII at 0.57 keV and O VIII at 0.65 keV, indicated by blue arrows).

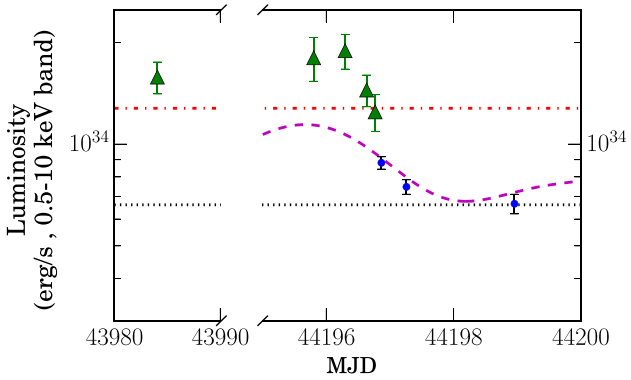

Figure 8. *Einstein*/HRI (green triangles) and *Einstein*/IPC (blue dots) observations of 47 Tuc in 1979 as reported by Auriere et al. (1989). Black dotted line shows the cumulative luminosity of X-ray sources in 47 Tuc's half-mass radius with X9 at minimum luminosity, and the red dash–dotted line shows the cumulative luminosity of the cluster with X9 at the maximum luminosity observed by *Chandra*/HRC. The dashed magenta line shows a projection of our Fourier fit to *Chandra*/HRC data (with arbitrary shift applied in time). HRI data points above the periodic profile and maximum observed luminosity indicate that an X-ray source in 47 Tuc was showing enhanced activity during *Einstein*/HRI observations.

The peak of the combined *Einstein* light curve, at $\sim 2 \times 10^{34}$ erg s^{-1}, was also well above the typical cluster luminosity, $\sim 5.7 \times 10^{33}$ erg s^{-1} for all sources besides X9 (Heinke et al. 2005b), and above the maximum cluster luminosity when X9 was at peak ($\sim 1.3 \times 10^{34}$ erg s^{-1}). However, the *Einstein*/IPC data show a decline in luminosity down to fluxes consistent with the rest of the cluster, plus X9 in its lower state, on time-scales typical of X9's variations (Fig. 8). The excellent match of the X-ray position, minimum flux and decay time-scale suggest that the bright state recorded by *Einstein*/HRI was due to X9, reaching a peak luminosity roughly twice the maximum luminosity seen by *ROSAT*, *Chandra* or *Swift* later.

3.2 X-ray spectroscopy

We tried to constrain the broad-band spectral shape through joint *Chandra* and *NuSTAR* spectral fitting. We used XSPEC 12.8.2 in all our spectral analysis and assumed Wilms, Allen & McCray (2000) abundances and Verner et al. (1996) cross-sections. Foreground reddening in the direction of 47 Tuc is $E(B-V) = 0.04$ (Salaris et al. 2007). Assuming $R_V = 3.1$ and using the observed correlation between extinction (A_V) and hydrogen column density $N_{\rm H}$ for Wilms abundances (Bahramian et al. 2015; Foight et al. 2016), we estimate a hydrogen column density of $3.5(\pm 0.1) \times 10^{20}$ cm^{-2}. We assumed this as the hydrogen column density towards 47 Tuc throughout this paper. Since $N_{\rm H}$ is quite small, variations in hydrogen column density (e.g. due to differential reddening) would lead to correspondingly small variations in spectral fits. For all spectral analyses, we considered 0.4–10-keV band data from *Chandra*/ACIS and 6.0–79-keV data for *NuSTAR*. Our *NuSTAR* spectra contain data from two observations (Table 1) and two modules (FPMA and FPMB), We fit all these spectra jointly (instead of combining the spectra). Due to the brightness of X9, we also accounted for the effects of pile-up on ACIS data by including the `pileup` model in XSPEC in all *Chandra* spectral fittings, even though the 2014–15 *Chandra*/ACIS campaign used a 1/8 sub-array mode to reduce pile-up (to less than 2 per cent). Due to possible differences in detector responses between *NuSTAR* and *Chandra*/ACIS, we include a variable coefficient in all our models representing the *NuSTAR*/*Chandra* relative normalization ratio.

The X-ray spectrum of X9 (Fig. 9) contains a strong line complex in 0.5–0.7 keV, attributed to O VII (at 0.57 keV) and O VIII (at 0.65 keV) by Heinke et al. (2005b), and an extended hard energy tail. We see no evidence of a Kα iron line. Our initial model for fitting the spectrum was an absorbed collisionally ionized gas model (`mekal`

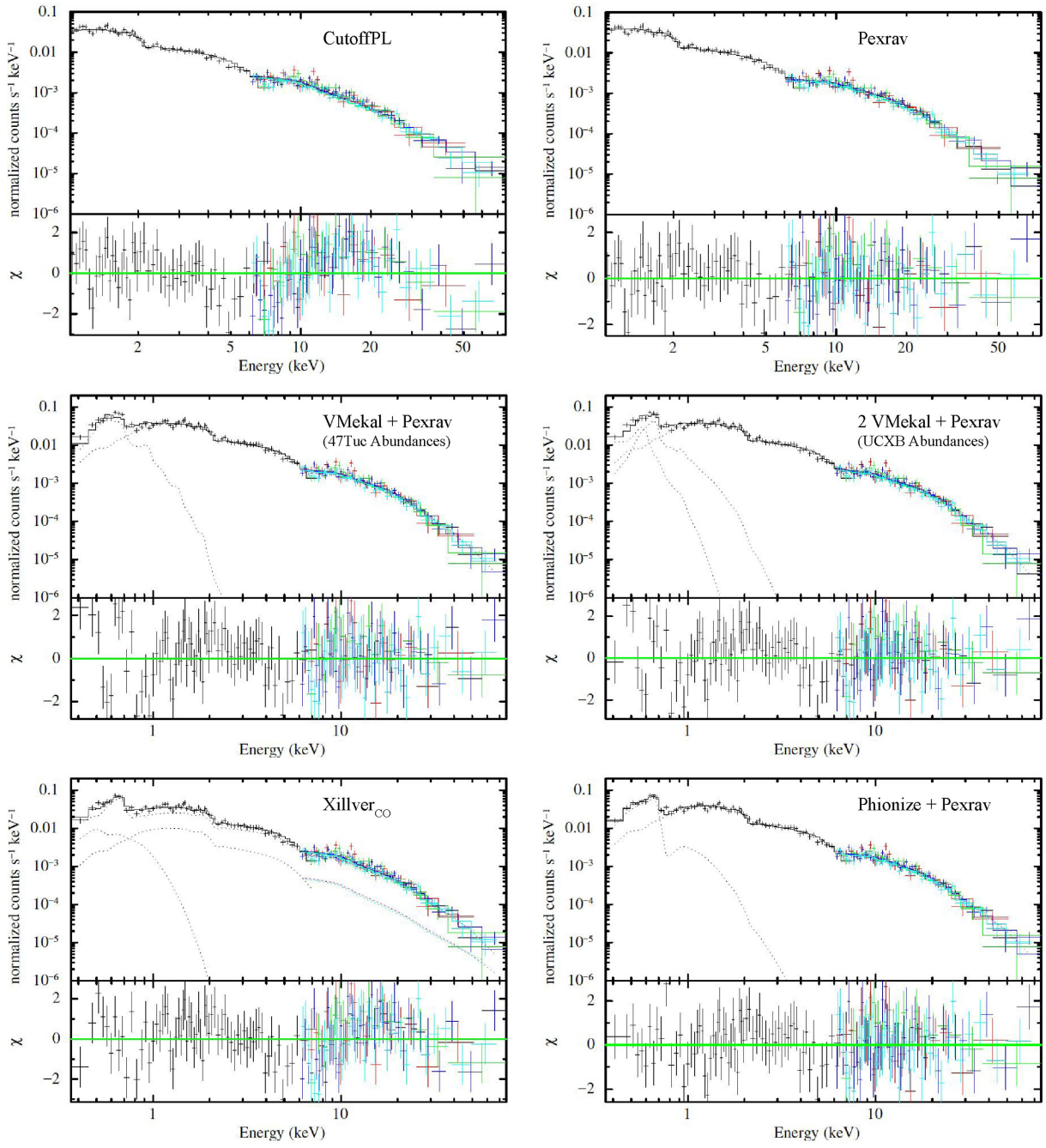

Figure 9. X-ray spectrum of 47 Tuc X9 as seen by *Chandra* (black) and *NuSTAR* (coloured, red and blue from FPMA, green and cyan from FPMB) in 2015 February and models used to fit the spectra. The top panels show two of the fits performed in the 1–79-keV band to address the reflection bump above 10 keV, and the middle and bottom panels show attempts to address the oxygen features below 1 keV. The models represented here are as follows: a cut-off power law (top-left), pexrav (top-right), a single vmekal + pexrav with 47 Tuc cluster abundances (mid-left), two vmekals+pexrav with UCXB abundances (mid-right), UCXB reflection model (bottom-left) and oxygen photoionization+pexrav (bottom-right). In the top panels, the reflection bump above 10 keV is clearly addressed by pexrav. Oxygen photoionization is the only model properly fitting the oxygen features below 1 keV.

model in XSPEC, e.g. Mewe, Gronenschild & van den Oord 1985; Mewe, Lemen & van den Oord 1986), plus a cut-off power law (`constant*pileup*tbabs*(mekal+cutoffpl)`).[9] However, this model failed to describe the spectra ($\chi^2_\nu = 1.56$ for 185 d.o.f). In particular, it failed to fit some of the stronger oxygen features below 1 keV. We discuss fit improvements for these features in detail in Sections 3.2.2, 3.2.3 and 3.2.4.

3.2.1 *Comptonization and reflection*

In addition to the low-energy features, our initial fit (`constant*pileup*tbabs*(mekal+cutoffpl)`) shows

[9] Note that the constant factor in the model represents the *NuSTAR*/*Chandra* normalization ratio.

Table 2. Best-fitting parameter values for hard spectral components, fit in the 1–79-keV band. T_0 is the temperature of the incident photons, T_e is the electron temperature and τ is optical depth in Comptonization models. We assume a disc geometry for the Comptonization component (CompTT). E_{fold} is the folding energy for exponential cut-off in the power-law tail. Reflection scale indicates the relative scale of the reflected emission compared to the source. Iron abundance is indicated as a fraction of solar abundance. The inclination angle is denoted by θ and ξ represents the ionization parameter. $C_{NU/CX}$ shows the relative *NuSTAR* to *Chandra*/ACIS normalization factor. N.H.P. indicates the null hypothesis probability.

	Without reflection		With reflection		
	Power law	CompTT	Pexrav	Pexriv	Reflect×CompTT
Photon index	1.01 ± 0.07	–	1.2 ± 0.1	$1.17^{+0.1}_{-0.03}$	–
E_{fold} (keV)	>85	–	56^{+22}_{-14}	62^{+63}_{-15}	–
T_0 (keV)	–	<0.3	–	–	0.35 ± 0.04
T_e (keV)	–	>161	–	–	62^{+234}_{-31}
τ	–	$1.8^{+1.3}_{-0.8}$	–	–	$0.9^{+2.7}_{-0.8}$
Reflect scale	–	–	$1.3^{+2.0}_{-0.4}$	$1.1^{+1.0}_{-0.3}$	$5.5^{+4.4}_{-1.8}$
Fe abund.	–	–	<0.3	<0.3	<0.3
θ°	–	–	<68	<45	<60
T_{disc} (keV)	–	–	–	$0.001\pm?^a$	–
ξ (erg cm s^{-1})	–	–	–	<270	–
$C_{NU/CX}$	1.03 ± 0.09	$1.07^{+0.09}_{-0.07}$	0.90 ± 0.09	$0.88^{+0.1}_{-0.09}$	$0.87^{+0.13}_{-0.06}$
χ^2_ν/d.o.f	1.37/171	1.39/170	0.98/168	0.99/166	1.00/167
N.H.P (per cent)	0.06	0.05	54.2	52.4	47.2

[a]The disc temperature in the Pexriv model is not constrained and the value stated here is just from the best fit.

a significant trend of residuals as a 'bump' in the 10–30-keV region (Fig. 9, top-left). Thus, we test other appropriate models by replacing the power-law component with them. To compare models in how they fit the harder part of the spectrum, in this section we report statistics in the 1-79-keV band for each model. Our initial power-law-only model yielded a χ^2_ν of 1.37 for 171 d.o.f. Replacing the power law with a Comptonization model (e.g. `compTT`; Titarchuk 1994) does not improve the fit (χ^2_ν of 1.39 for 170 d.o.f).

It is possible that the observed bump is caused by reflected emission. Replacing the power law with a reflected power law from neutral matter (`pexrav`; Magdziarz & Zdziarski 1995) improved the fit significantly ($\chi^2_\nu = 0.98$ for 168 d.o.f, Fig. 9, top-right). A reflected power law from ionized matter (`pexriv`) gives similar results ($\chi^2_\nu = 0.99$ for 166 d.o.f) but leaves the disc temperature and ionization parameter ($\xi = 4\pi F_{ion}/n$, where F_{ion} is irradiating flux in the 5–20-keV band and n is density of the reflector) mostly unconstrained ($\xi < 270$ erg cm s^{-1}). We also tried fitting the hard component of the spectrum using a Compton-scattering model convolved with a reflection model (e.g. `reflect*comptt`). This model also addresses the reflection bump well ($\chi^2_\nu = 1.00$ for 167 d.o.f). The details of our spectral fitting with these models are tabulated in Table 2.

The general improvement achieved by adding effects of reflection to the model, and the fact that the reflection scale parameter in all cases is non-zero (>0.5), gives strong evidence for the significance of reflection in this system.

All three models containing reflection fit the spectrum well. We prefer a non-ionized reflecting material, as the ionization parameter in Pexriv is loosely constrained and is consistent with zero (i.e. suggesting insignificance of ionized matter in the reflection). As the physically motivated model (reflect×compTT) requires an unusually high reflection scale parameter, indicating significant obscuration of the emission source (which seems inconsistent with the constraints on the inclination angle in the reflection component), we use Pexrav for the rest of our analysis.

3.2.2 *Collisionally ionized gas models*

After addressing the hard component of the spectrum, we focused on the features in the soft end while fitting the whole band (0.4–79.0 keV). Our model with a single Mekal model and pexrav (`constant*pileup*tbabs*(mekal+pexrav)`) failed to describe the strong emission features below 1.0 keV ($\chi^2_\nu = 1.34$ for 183 d.o.f) leaving significant residuals below 1 keV. Adding a second mekal component did not improve the fit. As the features we are trying to fit are dependent on the abundances of elements in the system, we test our model with 47 Tuc abundances of elements (following Heinke et al. 2005b, assuming linear abundance of 60 per cent solar for C, N and O, 40 per cent solar for elements Ne through Ca, and 20 per cent solar for Fe and Ni; see also Carney 1996; Salaris & Weiss 1998). To do so, we replace the Mekal component in our model with VMekal, which allows for adjustable abundances of elements. This model provides a slightly better fit with a $\chi^2_\nu = 1.23$ for 183 d.o.f (Fig. 9, middle-left). Adding a second vmekal component did not improve the fit.

The major features that the models above fail to describe mainly consist of strong spectral lines, from O VII and VIII between 0.6 and 0.8 keV (Fig. 10). Additionally, in our *Chandra*/ACIS spectrum, there is a bump at ∼0.3 keV, which is not fit well when our band is extended to 0.3 keV. This bump could be due to uncertainties in the ACIS response matrix, or could be due to carbon lines. This is particularly plausible as Knigge et al. (2008) identify strong carbon lines in the FUV spectrum of X9. This significant underestimation of oxygen emission in our models suggests that the abundance of oxygen (and possibly carbon) in this system is higher than both the measured values for 47 Tuc, and solar abundances. Miller-Jones et al. (2015) suggest that X9 might be a UCXB (based on mass-transfer rate). This is consistent with possibly high abundance of oxygen, as in UCXBs where the donor is a C/O WD, carbon and oxygen can be dominant species. We attempt a first test of this scenario by using the abundances calculated by Koliopanos, Gilfanov & Bildsten (2013) for a C/O UCXB system. Although a model with

Table 3. Best-fitting parameter values for our models fitting the entire 0.4–79-keV band spectrum. The VMekal models are VMekal+pexrav models with abundance of elements based on values for solar (Wilms et al. 2000), 47 Tuc (Carney 1996; Salaris & Weiss 1998; Heinke et al. 2005b) and UCXB abundances (Koliopanos et al. 2013). Phoionize is the oxygen photoionization model produced using XSTAR (see text). *T*1 and *T*2 are temperature of each Mekal/VMekal component. Adding a second VMekal component only improved the fit in the case with UCXB abundances. In the case of Phoionize, *T*1 is the temperature of the photoionized region. $E_{\rm fold}$ represents the exponential cut-off energy in Pexrav and θ the inclination angle. For the C/O Phoionize model, we found the best-fitting value for carbon to oxygen abundance ratio to be 0, however the value is unconstrained and the uncertainty estimation reaches the model hard limit of 2. Note that the iron abundance parameter in Pexrav is set to the value assumed for VMekal in each case. For Phoionize, this parameter was set free and was found to be <0.3 of the solar value in both cases.

	VMekal			$\text{Xillver}_{\rm CO}$	Phoionize	
	Solar	47 Tuc	UCXB	UCXB	Oxygen	C/O
*T*1 (keV)	0.16 ± 0.01	$0.17^{+0.01}_{-0.02}$	0.26 ± 0.05	0.11 ± 0.01	$0.20^{+0.08}_{-0.10}$	$0.24^{+0.05}_{-0.11}$
*T*2 (keV)	–	–	<0.3	–	–	–
$\log(\xi)$	–	–	–	–	$0.6^{+0.8}_{-0.1}$	$0.3^{+0.1}_{-0.5}$
Photon index	1.04 ± 0.08	1.07 ± 0.08	1.05 ± 0.08	$1.2^{+0.3}_{-0.2}$	$1.12^{+0.08}_{-0.07}$	$1.10^{+0.07}_{-0.08}$
$E_{\rm fold}$ (keV)	35^{+13}_{-7}	47^{+14}_{-9}	38^{+12}_{-7}	201 ± 15	51^{+18}_{-11}	49^{+17}_{-11}
Reflect scale	$1.3^{+3.0}_{-0.5}$	$1.1^{+1.5}_{-0.4}$	$1.2^{+2.0}_{-0.4}$	–	$1.1^{+1.5}_{-0.3}$	$1.1^{+1.4}_{-0.4}$
θ (deg)	<78	<68	<72	<54	<66	<46
$\text{Norm}_{\rm NU/CX}$	$0.96^{+0.09}_{-0.08}$	$0.90^{+0.09}_{-0.08}$	0.93 ± 0.08	$1.00^{+0.06}_{-0.07}$	0.89 ± 0.09	0.88 ± 0.09
χ^2_ν/d.o.f	1.33/183	1.23/183	1.22/181	1.30/181	1.02/181	1.03/180
N.H.P (per cent)	0.15	1.8	2.1	0.43	41.6	36.0

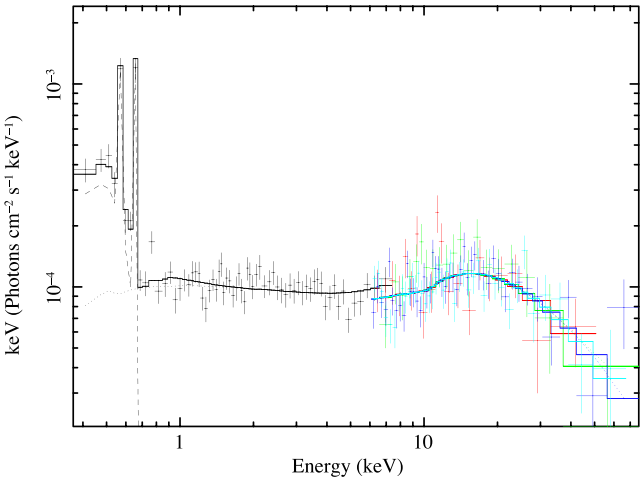

Figure 10. Unfolded best-fitting model (oxygen photoionization+pexrav) describing X-ray spectrum of X9 and the oxygen lines in the system. *Chandra* data and fit shown in black and *NuSTAR* in coloured (red and blue from FPMA, green and cyan from FPMB). The dashed line represents the photoionization component, while the dotted line indicates the Pexrav reflection component. The dominant oxygen lines are O VII at 0.57 keV and O VIII at 0.65 keV.

a single VMekal component with UCXB abundances fails to describe the features below 1 keV ($\chi^2_\nu = 1.35$ for 183 d.o.f), adding a second VMekal component gives a slightly better fit with $\chi^2_\nu = 1.22$ for 181 d.o.f. (Table 3 and Fig. 9, middle-right). The slight improvement in the fit and the less-structured appearance of the residuals suggests a C/O WD companion in this system.

3.2.3 *Reflection models for UCXBs*

Our spectral analysis in Sections 3.2.1 provides evidence for reflection, and Section 3.2.2 indicates an ultracompact nature for the system, with a high abundance of oxygen. Thus, it is possible that the strength of oxygen lines is due to reflection from a hot, oxygen-rich disc. We test this scenario by fitting the spectrum with a reflection model appropriate for oxygen-rich UCXBs.[10] For this purpose, we used $\text{Xillver}_{\rm CO}$ (Madej et al. 2014), which is a reflection model for accretion discs in oxygen-rich UCXBs. $\text{Xillver}_{\rm CO}$ is based on the Xillver reflection model (García & Kallman 2010; García, Kallman & Mushotzky 2011; García et al. 2013).

$\text{Xillver}_{\rm CO}$ contains only the *reflected* emission from a disc plus a power-law continuum (and not the emission from these components themselves). Thus, to include all the components, our model became `constant*pileup*tbabs*(diskbb+cutoffpl+xillverCO)`. In this model, we tied the disc temperature between $\text{Xillver}_{\rm CO}$ and diskbb, and tied the photon index and cut-off energy between $\text{Xillver}_{\rm CO}$ and the cut-off power law. This model gives a moderate fit with $\chi^2_\nu = 1.30$ for 181 d.o.f. However, it shows clear residuals in fitting the oxygen features and the reflection bump (Fig. 9, bottom-left).

3.2.4 *Photoionized gas models*

None of the models tested in Sections 3.2.2 and 3.2.3 seem to be able to entirely address the oxygen features. Specifically, most of these models seem to underestimate the relative amplitude of O VIII compared to O VII (these lines are demonstrated in Fig. 10). This could be due to significant increase in the ionization state of oxygen due to photoionization. To investigate this, we used XSTAR (Kallman & Bautista 2001) to simulate a model spectrum of photoionized oxygen in a system with a size scale applicable to X9. XSTAR is designed to self-consistently simulate emission and absorption by hot, diffuse gas. We assume that the diffuse gas surrounds the system and is illuminated by the inner accretion flow.

For our simulations, we considered two scenarios: (i) a diffuse gas region filled with just carbon and oxygen, and (ii) a purely oxygen diffuse gas region. In both cases, we assumed the gas is illuminated

[10] None of the standard reflection models incorporated within XSPEC consider hydrogen-deficient gas.

by a source (possibly the inner accretion flow) with an X-ray luminosity of $\sim 10^{33}$ erg s^{-1} (a typical luminosity level for X9). For the illuminating source, we assumed a power-law spectrum obtained from the best power-law fit to the *Chandra*/ACIS spectrum in the 1–10-keV band (with a photon index of 1.1 and a 0.5–10-keV flux of 1.4×10^{-12} erg s^{-1} cm^{-2}). For the simulations, we assumed a hydrogen column density of 10^{22} cm^{-2} and a constant gas density of 10^{10} cm^{-3}. While quick tests indicate our results do not appear to be highly sensitive to these parameters, we will investigate a broader range for these parameters in future work. The variables in our grid model were temperature (10^4–10^7 K), ionization parameter[11] ($\log \xi$ from -4 to 4) and in the case of the C/O gas, relative abundance of carbon compared to oxygen (from 0 to 2). Our simulations were parallelized using PVM_XSTAR (Noble et al. 2009). Finally, we produced XSPEC table models using the XSTAR task `xstar2table` and performed spectral fitting with these models. From here on, we refer to these models as the photoionization model (`phoionize`).

We used a slightly different version of XSTAR (2.2.1bo8) compared to the regular XSTAR release (2.2.1bn24). The main difference between the two versions is the effects of bound–bound radiative excitation, which is turned on in the 2.2.1bo8 release. This is especially important as the oxygen Lyα line can also be emitted by bound–bound radiative excitation of the upper level by continuum photons. Thus, the 2.2.1bo8 release produces the helium-like oxygen line at a different energy as it pumps the resonance line, while the regular version makes a stronger intercombination line via recombination.

We used our XSTAR models to fit the joint *Chandra* and *NuSTAR* spectra. To do so, our full model became `constant*pileup*tbabs*(phoionize+pexrav)`. This model fit the spectra exceptionally well with $\chi^2_\nu = 1.02$ for 181 d.o.f in the case of pure-oxygen and $\chi^2_\nu = 1.03$ for 180 d.o.f in the case of C/O (Table 3), almost completely removing residuals around the oxygen features (Fig. 9, bottom-right). Our best fit using the oxygen-only model gives a gas temperature of $0.20^{+0.08}_{-0.10}$ keV and an ionization parameter ($\log \xi$) value of $0.6^{+0.8}_{-0.1}$. The best fit with the C/O model gives a similar fit with a gas temperature of $0.24^{+0.05}_{-0.11}$ keV, ionization parameter ($\log \xi$) of $0.3^{+0.1}_{-0.5}$ and ratio of carbon/oxygen abundance consistent with zero (unconstrained however). With both models, in our best fits, the Fe abundance in Pexrav is found to be <0.3 of the solar value. Koliopanos et al. (2013) suggest that strength of Fe Kα line (and thus, measured abundance of iron) should be suppressed in systems with high carbon and oxygen abundances. However, Madej et al. (2014) indicate that this is only the case in systems with completely neutral gas. The goodness of fit for the `phoionize` model clearly indicates present of an ionized region in the system (dominated by oxygen and carbon). However, we do not see any evidence for a Fe Kα line in the spectrum of X9. This could mean that the accretion disc is nearly neutral and the ionized gas is not part of the disc. It could also mean that the Fe abundance is much lower than solar. This is not surprising as Fe abundance is expected to be low for a 47 Tuc donor star even if not a WD.

We are certain that C exists in the accretion disc, since a strong double-peaked C IV line is detected in the UV spectrum (Knigge et al. 2008) but no C lines fall into our X-ray fitting range (as they lie below 0.5 keV). We will address constraints on the C/O abundance ratio in a future paper. Using a pure O model gives a good fit, and should not produce significantly different results from the full C/O models (either in goodness of the fit or parameter values) for the spectral fitting range we consider.

Reproducing our models using the 2.2.1bn24 version of XSTAR yielded an inferior fit ($\chi^2_\nu = 1.2$ compared to 1.02 for 2.2.1bo8, both for 181 d.o.f). This result indicates the importance of bound–bound radiative excitation in production of these lines in the emitting region.

Although our photoionized model provides a very good fit, there is a single spectral bin around $\sim$0.8 keV that shows a significant residual (Fig. 9, bottom right). As this spectral bin is located in a region where the dominant component changes, it is unclear if this residual is due to incomplete modelling of the underlying continuum or caused by a spectral feature. The final model that best fits the spectra is plotted in Fig. 10.

The superiority of this fit compared to the collisional models discussed in the previous section is a strong indicator of the extreme overabundance of oxygen and the fact that photoionization in this system is not negligible. We discuss the implications of this finding in Section 4.1.

Our spectral analysis presented above is a first glance at a complex system. We note that in other *Chandra* data sets, due to the strong presence of oxygen features, Mekal with UCXB abundances or our photoionized model fits the spectra significantly better than models with solar abundances. We found our model fits most of the *Chandra* spectra reasonably well; however, we also noticed significant residual trends in a few data sets. We leave extensive spectral modelling and an in-depth study of the spectral evolution in the system to a later paper (Bahramian et al., inpreparation).

4 DISCUSSION

4.1 X9 as an ultracompact X-ray binary

Based on the X-ray luminosity of X9 ($L_X \sim$ a few $\times 10^{33}$ erg s^{-1}) and the inferred mass-transfer rate, Miller-Jones et al. (2015) suggested the system might be a UCXB with an orbital period of $\sim$25 min. Knigge et al. (2008) reported the presence of strong carbon lines in the UV spectrum of X9, indicating the presence of carbon in the accretion flow, and absence of helium lines (hinting at the possibility of a C/O WD donor).

We detect a significant periodic signal in the X-ray light curve with a period of 28.18 ± 0.02 min. This signal is likely the orbital period of the system, indicating that X9 is a UCXB. It is worth noting that this periodic signal is mainly present in the 0.5–0.7-keV band dominated by the O VII and VIII lines. This could be foreground column variation due to a disc wind. Since such a foreground column is probably almost pure C/O, there can be a relatively weak wind and it can still provide a significant absorption column, especially in the oxygen edge.

Heinke et al. (2005b) showed that in X-rays, X9's spectrum contains strong oxygen lines below 1 keV. As we tried to model the spectrum with various models (collisional gas, reflection in UCXBs, and oxygen photoionization; Section 3.2), we find the oxygen photoionization model to provide a clearly better fit compared to the rest of the models. The superior goodness of this fit indicates the significance of photoionization in production of these oxygen lines, and thus points to the presence of overabundant oxygen, possibly in the form of a diffuse region around the inner accretion disc. Clear evidence of photoionized oxygen excess provides additional evidence for a C/O WD companion in this system.

[11] Note that this ionization parameter is defined as $\xi = L/nR^2$ where L is luminosity, n is density and R is distance from the illuminating source.

Our best-fitting model (Section 3.2) indicates the presence of an exponentially cut-off power law, which dominates the emission above 1 keV. This component is most likely associated with the inner optically thin accretion flow. However, the fit with the cut-off power law shows correlated residuals in the 10–30-keV band. These residuals largely disappear when a reflection model is convolved with the cut-off power-law. This strongly indicates the presence of reflected emission from an optically thick accretion disc, possibly located further out from the accretor. However, direct X-ray emission from this accretion disc (e.g. a disc blackbody) is not visible, as expected given the low X-ray luminosity of the system. The reflected cut-off power law described all the emission above 1 keV. However, there are strong emission lines below 1 keV that this model fails to describe. These lines are associated with oxygen VII and VIII and seem to be described by photoionization (rather than collisional models). Our best-fitting model suggests that these lines are produced within an oxygen-rich diffuse gas region possibly embedding the inner parts of the system and irradiated by the accretion flow. The overabundance of oxygen required to explain these lines suggests a hydrogen-poor companion, thus pointing at the ultracompact nature of the system.

4.2 Nature of the compact accretor

Our radio observation of X9 measured flux densities of 27.6 ± 7.2 and 30.7 ± 8.9 μJy bm^{-1} at 5.5 and 9.0 GHz, respectively. Comparing with previous observations in 2010 and 2013 (Miller-Jones et al. 2015), the 9-GHz radio emission has not changed markedly since the prior observations, although the 5.5-GHz emission appears to have dropped by a factor of 1.5 ± 0.4. Despite the poor weather and low elevation of X9 for much of the observation, we found no significant evidence for phase decorrelation in the other sources in the field, when comparing their measured fluxes with those determined from the 2010 and 2013 data.

Is it possible to explain X9 as a CV? Looking simply at the radio, X-ray and optical fluxes of X9, we see that X9 would be extremely unusual among CVs in its radio flux, its X-ray flux and its X-ray to optical flux ratio. X9 would have the highest radio flux of any observed CV (e.g. see Coppejans et al. 2016; Mooley et al. 2017; Russell et al. 2016), and maintains this high radio flux in two widely separated quiescent epochs, in contrast to other CVs, which reach their peak radio brightness during short-lived epochs.

The X-ray flux of X9 is similar to that of the most X-ray luminous known CVs, which reach $L_{\rm X}(0.5–10\ {\rm keV}) \sim 5 \times 10^{33}$ erg s^{-1} (e.g. see Stacey et al. 2011; Bernardini et al. 2012; Pretorius & Mukai 2014). These systems are all known (or thought) to be intermediate polars, which channel the accretion flow via their magnetic field to the poles, producing shocks above the WD surface (e.g. Aizu 1973). This enables strongly magnetic CVs to avoid producing an optically thick boundary layer as in non-magnetic CVs, which shifts the majority of the accretion luminosity into the ultraviolet range (Patterson & Raymond 1985).

However, X-ray luminous intermediate polars have orbital periods of 3.4–10 h (or more), producing mass-transfer rates of $\sim 10^{-8}$ M$_\odot$ yr^{-1} (e.g. Howell 2001). For a 1-M$_\odot$ WD, this gives $L_{\rm bol} \sim 1.5 \times 10^{35}$ erg s^{-1}, allowing them to produce X-ray luminosities of a few 10^{33} erg s^{-1} even though most of the released luminosity is not in this energy band (e.g. Evans et al. 2009). We have strong evidence for X9's orbital period being 28 min, which indicates a mass-transfer rate of 2×10^{-11} M$_\odot$ yr^{-1} for a C/O donor (Deloye & Bildsten 2003); for a typical intermediate polar conversion efficiency of mass transfer into X-ray luminosity of 2 per cent, we would then expect $L_{\rm X} \sim 6 \times 10^{30}$ erg s^{-1}, and (implausibly) perfect conversion efficiency would give $L_{\rm X} = 3 \times 10^{32}$ erg s^{-1}. Increasing the WD mass to the maximal 1.4 M$_\odot$, and assuming perfect conversion efficiency, is required in order to reach $L_{\rm X} = 2 \times 10^{33}$ erg s^{-1}.

One could also contrive a scenario in which the orbital period is around 10 min (producing a mass-transfer rate of 10^{-8} M$_\odot$ yr^{-1} as in known intermediate polars, using the evolutionary tracks of Deloye & Bildsten 2003), and the accretion is magnetically channelled to the surface, permitting a large hard X-ray luminosity; but this would require that the true spin and orbital periods of a strongly magnetic WD remain undetected, while a spurious 28-min period is produced, and an extremely high radio flux is produced. Both of these scenarios appear extremely improbable.

With our simultaneous X-ray and radio measurements of X9 from 2015 February, we plot X9 on the $L_{\rm R}$–$L_{\rm X}$ plane (Fig. 11). Compared to Miller-Jones et al. (2015), we find a lower 5.5-GHz luminosity, but a higher X-ray luminosity.[12] This places X9 within the scatter of the BH population (and near the track followed by XTE J1118+480; Gallo et al. 2014), but closer to the tMSPs.

The position of X9 on the $L_{\rm R}$–$L_{\rm X}$ plot rules out a CV but cannot discriminate between an (tMSP) NS or a BH as possibilities for the accreting object. There have only been 10 quiescent BH LMXBs with detailed X-ray analyses (Plotkin, Gallo & Jonker 2013), and only ∼3–4 quiescent BH LMXBs with deep radio/X-ray studies (e.g. Plotkin et al. 2016). The X-ray properties of X9 are significantly different from those of any known tMSP or BH LMXB. X9 has a significantly harder continuum spectrum than either tMSPs (photon indices 1.5–1.7; de Martino et al. 2010; Linares et al. 2014; Bogdanov & Halpern 2015; Bogdanov et al. 2015) or BH LMXBs in quiescence (photon indices in the range 1.5–2.3; Plotkin et al. 2013; Wijnands et al. 2015). It is worth noting that tMSPs in rotation-powered state can show a hard spectrum (with photon index ∼1.1; de Martino et al. 2015). However, X9 is too bright (both in radio and X-rays) to be in this state. Fitting X9's 0.5–10-keV spectrum (in sub-array mode to eliminate pile-up) gives a photon index of 1.06 ± 0.24 (Miller-Jones et al. 2015). We might tentatively speculate that X9's unusual continuum spectral shape might be related to the unusual chemical composition of its donor. Similarly, the 6.8-d order-of-magnitude variation in X9's X-ray flux is not similar to any behaviour seen in either tMSPs or BH LMXBs. Detection or ruling out pulsations would be strong evidence, but the pulsed fraction limit of <19 per cent that we were able to set from the *Chandra* HRC data alone cannot rule out a tMSP nature, since for some tMSPs the coherent X-ray pulsations have pulsed fractions down to 8 per cent (Archibald et al. 2015; Papitto et al. 2015). Detection of a sharp change in the *Fermi* gamma-ray flux from 47 Tuc coincident with a state change in X9 would also be a strong signal that X9 is a tMSP (Stappers et al. 2014; Johnson et al. 2015). No such change is visible in the long-term *Fermi* light curves from 47 Tuc, but this is not strongly constraining considering the presence of >20 gamma-ray-emitting MSPs in the cluster (e.g. Camilo et al. 2000; Freire et al. 2003; Abdo et al. 2009; Pan et al. 2016; Ridolfi et al. 2016).

An inspection of its variability properties shows X9 to behave somewhat differently to the known tMSPs in both the radio and X-ray bands, although we note that the samples of well-studied tMSP and quiescent BH sources are both small. First, the three verified tMSPs (and a candidate tMSP) show rapid (hundreds to thousands of seconds) switching between two relatively stable luminosity

[12] Note that the observations reported in Miller-Jones et al. (2015) were not simultaneous.

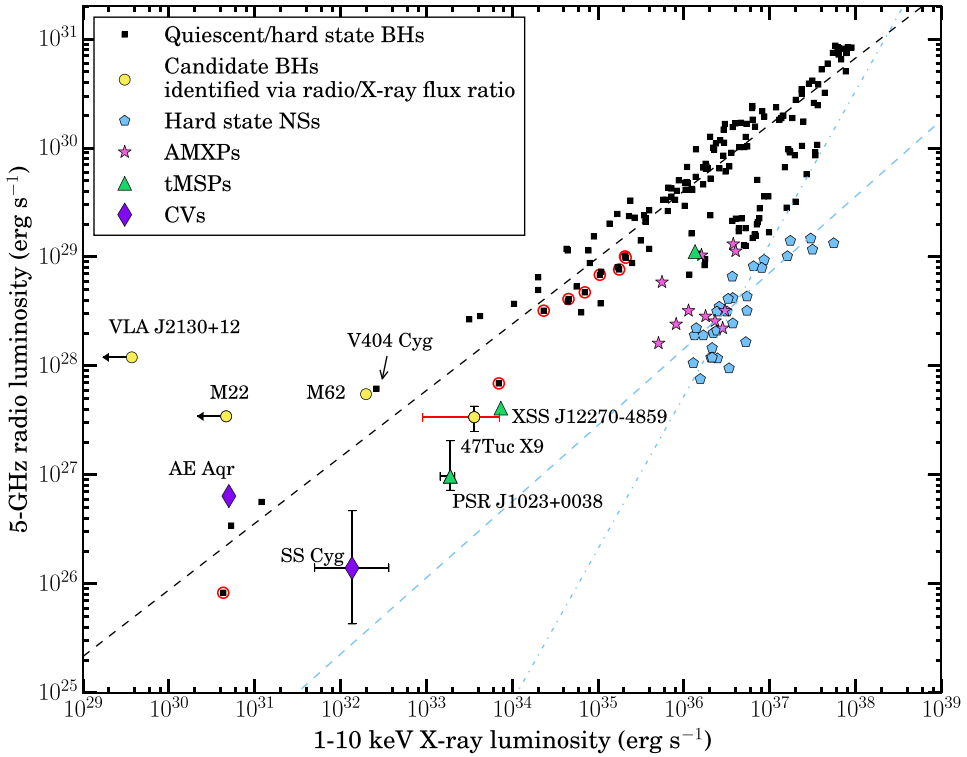

Figure 11. Radio/X-ray luminosity correlation for XRBs and stellar mass BHs. Plot adapted from Tetarenko et al. (2016). X9 falls below the correlation line for BH LMXBs, but consistent with the observed track of XTE J1118+480 (Gallo et al. 2014, denoted by red circles around black squares in this plot). Note that the uncertainty on X-ray luminosity of 47 Tuc X9 is relatively small ($\sim 3 \times 10^{31}$ erg s^{-1}) and the red bar in this plot just demonstrates the scale of X-ray variability. The data point for SS Cyg and AE Aqr show their radio and X-ray luminosities during their flaring states (Russell et al. 2016).

levels around 10^{33} and 10^{34} erg s^{-1} (de Martino et al. 2013; Papitto et al. 2013; Linares et al. 2014; Tendulkar et al. 2014; Bogdanov & Halpern 2015; Bogdanov et al. 2015). However, Miller-Jones et al. (2015) were able to show that the available X9 X-ray data does not show sudden dips to a 'low mode', or rapid flaring states, as seen in the X-ray light curves of the three known tMSPs (de Martino et al. 2013; Linares et al. 2014; Bogdanov & Halpern 2015); of order 100 detectable drops to the 'low mode' should have been detected in the X9 *Chandra* data, should it show a similar distribution of 'low-mode' dip frequency with dip length (e.g. dips longer than 200 s on average every 3 ks) as PSR J1023+0038 or XSS J12270−4859.

Secondly, X9's radio flux appears quite stable (varying by less than a factor of 3) between different observing epochs (10-h runs in 2010 and 2013, and 12 h in 2015). This is in contrast to PSR J1023+0038, which shows dramatic variations of up to a factor of 100, varying by a factor of 10 on as short a time-scale as 30 min (Deller et al. 2015). Such strong variations in the radio have not been seen from BH LMXBs in quiescence (see, e.g., Hynes et al. 2004; Miller-Jones et al. 2008; Gallo et al. 2014). Thus, X9 would appear more similar to BH LMXBs in both its X-ray and radio variability properties than to tMSPs. However, with only three tMSPs confirmed so far, we cannot be certain that all tMSPs will show the same patterns of X-ray and radio variability as the known sources, so we cannot rule out a tMSP as a possibility, but the evidence suggests a moderate preference for a BH nature of the accretor.

An alternative scenario is that we are viewing the system at a very high inclination angle, where the outer disc obscures the inner parts of the accretion disc, so that the observed X-ray flux is significantly lower (∼2–3 orders of magnitude) than the true flux. We found clear evidence for reflected emission in the X-ray spectrum of X9. To our knowledge, this is the lowest luminosity XRB (non-CV) system to show reflection. Clear detection of reflection from a faint ($<10^{34}$ erg s^{-1}) system and the ionized emission possibly associated with an accretion disc corona in the system, dominating the continuum below 1 keV, suggests that the inner accretion disc might be heavily obscured and thus the true X-ray luminosity could be higher. In this scenario, an NS nature for the compact object would be preferred by the radio/X-ray flux ratio. We note that this case requires a very high inclination angle, which is inconsistent with the constraints indicated by the reflection models (Table 2). However, due to assumptions of the abundances of elements in these models (which do not consider hydrogen-deficient gas), these constraints could be inaccurate. In this scenario, the system is persistently bright, at an X-ray luminosity of $\sim 10^{36}$ erg s^{-1}, which is indeed consistent with the time-averaged mass-transfer rate for an NS XRB in a 28-min orbital period (Deloye & Bildsten 2003; van Haaften et al. 2012). However, we find no evidence for eclipses, while partial eclipses of the scattering region are invariably seen in such accretion disc corona sources (e.g. White & Holt 1982; Frank, King & Lasota 1987). The variability seen at 28 min takes far too much of the orbit to be an eclipse from a companion. Thus, we find the scenario of a very high inclination angle to be less plausible than the tMSP or BH LMXB models discussed above.

4.3 Origin of the superorbital periodicity

As discussed by Miller-Jones et al. (2015), the relatively high quiescent X-ray luminosity of X9 suggests a relatively high mass-transfer rate, only slightly below the rate needed to maintain the disc in a

persistently bright state. Such a high mass-transfer rate could be reached through standard binary evolution of a low-mass companion either at large orbital periods (such as the 6.5-d orbital period of V404 Cyg; Casares, Charles & Naylor 1992), or short orbital periods around 25 min. However, as discussed by Miller-Jones et al. (2015), any orbital periods larger than 3 h are clearly ruled out based on the limits on optical emission from the companion star. This paper presents robust evidence for a WD companion in the system (strong oxygen emission lines, and a periodic signal at 28.18 min). Thus, the 6.8-d periodicity, if real, must have a superorbital origin.

Superorbital modulations have been observed in multiple XRBs (e.g. see Charles et al. 2008 for a review). It is thought that these modulations can be produced by mechanisms like precession, tilting or warping of the accretion disc.

If this superorbital period is due to superhump precession, using the orbital period of $P_{\rm orb} = 28.2$ min and taking a precession period of $P_{\rm pre} = 6.8$ d, we can estimate the mass ratio q, using the relation $q = 0.114 + 3.97 \times (\epsilon - 0.025)$, where ϵ is the superhump excess and can be approximated by $P_{\rm orb}/P_{\rm pre}$ (Knigge 2006). Using this relation, we find $q \sim 0.026$. A UCXB with an orbital period of 28.2 min indicates a donor WD mass of $\sim 0.02\,{\rm M}_{\odot}$ (e.g. Rappaport et al. 1987) and thus suggests an accretor mass of $\sim 1\,{\rm M}_{\odot}$. We note that there are many uncertainties in this calculation; the superhump relations are derived empirically based on CVs, and are not validated for such low q values. If correct, this calculation would argue for an NS accretor; however, since we are not certain the 6.8-d periodicity is indeed periodic, that it is due to precession, or that the precession is necessarily due to the superhump instability, we cannot consider it strong evidence on the nature of the accretor. However, this calculation does indicate that a 6.8-d precession period is physically reasonable for a system with an orbital period of 28.2 min.

Among the systems showing superorbital modulation, 4U 1916−053 is a persistent UCXB (∼1000 times brighter than X9) with an orbital period of 50 min (Walter et al. 1982; Nelemans & Jonker 2010). Strong helium and nitrogen lines in the spectrum indicate an He WD companion (Nelemans, Jonker & Steeghs 2006), and X-ray bursts indicate an NS accretor (Becker et al. 1977). The short orbital period (1.8 h) system UW CrB (MS 1603+2600) shows a superorbital modulation of period ∼5 d (Mason et al. 2008; Hakala et al. 2009), presumably related to the 'superhump' phenomenon (Patterson et al. 2005). Charles et al. (2008) suggest that the 5-d modulation in this system[13] is caused by precession and/or warping of the accretion disc. Given the similarities between UW CrB and 47 Tuc X9, it is possible that similar mechanisms are responsible for the 6.7-d modulation observed in X9.

ACKNOWLEDGEMENTS

AB thanks E. W. Koch for help with computational aspects of this project, K. A. Arnaud for helpful discussion on spectral analysis and B. E. Tetarenko for help with the radio/X-ray luminosity plot. The authors thank F. A. Harrison for granting *NuSTAR* director's discretionary time for these observations and J. Tomsick for assisting in coordination of *NuSTAR* observations. JCAM-J is the recipient of an Australian Research Council Future Fellowship (FT 140101082). JS acknowledges support of NSF grant AST-1308124 and a Packard Fellowship. COH and GRS acknowledge support from NSERC Discovery Grants, and COH also acknowledges support from a Humboldt Fellowship. This work was funded in part by NASA *Chandra* grant GO4-15029A awarded through Columbia University and issued by the *Chandra* X-ray Observatory Center, which is operated by the Smithsonian Astrophysical Observatory for and on behalf of NASA under contract NAS8-03060.

The scientific results reported in this article are based on observations made by the *Chandra* X-ray Observatory, *NuSTAR* observatory and Australia Telescope Compact Array, and archival data obtained from *Chandra* and *Swift* data archives. The Australia Telescope Compact Array is part of the Australia Telescope National Facility, which is funded by the Australian Government for operation as a National Facility managed by CSIRO.

We acknowledge use of the following packages/softwares for analysis: the NuSTAR Data Analysis Software (NUSTARDAS) jointly developed by the ASI Science Data Center (ASDC, Italy) and the California Institute of Technology (Caltech, USA); CIAO, provided by the *Chandra* X-ray Center (CXC); HEASOFT, provided by the High Energy Astrophysics Science Archive Research Center (HEASARC), a service of the Astrophysics Science Division at NASA/GSFC and of the Smithsonian Astrophysical Observatory's High Energy Astrophysics Division; PVM_XSTAR, developed at the MIT Kavli Institute for Astrophysics and funded in part by NASA and the Smithsonian Institution, through the AISRP grant NNG05GC23G and Smithsonian Astrophysical Observatory contract SV3-73016; ASTROPY (Astropy Collaboration et al. 2013); ASTROML (Vanderplas et al. 2012); GATSPY (Vanderplas 2015); and MATPLOTLIB (Hunter 2007). Our simulations were performed using Cybera cloud computing resources (http://www.cybera.ca/). We acknowledge extensive use of NASA's Astrophysics Data System and Arxiv.

REFERENCES

Abdo A. A. et al., 2009, Science, 325, 845
Aizu K., 1973, Prog. Theor. Phys., 49, 1184
Alpar M. A., Cheng A. F., Ruderman M. A., Shaham J., 1982, Nature, 300, 728
Archibald A. M. et al., 2009, Science, 324, 1411
Archibald A. M. et al., 2015, ApJ, 807, 62
Arnaud K. A., 1996, in Jacoby G. H., Barnes J., eds, ASP Conf. Ser. Vol. 101, Astronomical Data Analysis Software and Systems V. Astron. Soc. Pac., San Francisco, p. 17
Astropy Collaboration et al., 2013, A&A, 558, A33
Auriere M., Koch-Miramond L., Ortolani S., 1989, A&A, 214, 113
Bachetti M. et al., 2014, Nature, 514, 202
Bahramian A., Heinke C. O., Sivakoff G. R., Gladstone J. C., 2013, ApJ, 766, 136
Bahramian A. et al., 2014, ApJ, 780, 127
Bahramian A., Heinke C. O., Degenaar N., Chomiuk L., Wijnands R., Strader J., Ho W. C. G., Pooley D., 2015, MNRAS, 452, 3475
Bailyn C. D., Grindlay J. E., 1990, ApJ, 353, 159
Becker R. H., Smith B. W., Swank J. H., Boldt E. A., Holt S. S., Serlemitsos P. J., Pravdo S. H., 1977, ApJ, 216, L101
Bernardini F., de Martino D., Falanga M., Mukai K., Matt G., Bonnet-Bidaud J.-M., Masetti N., Mouchet M., 2012, A&A, 542, A22
Bogdanov S., Halpern J. P., 2015, ApJ, 803, L27
Bogdanov S. et al., 2015, ApJ, 806, 148
Bogdanov S., Heinke C. O., Özel F., Güver T., 2016, ApJ, 831, 184
Bozzo E. et al., 2011, A&A, 535, L1
Burrows D. N. et al., 2005, Space Sci. Rev., 120, 165
Cameron P. B., Rutledge R. E., Camilo F., Bildsten L., Ransom S. M., Kulkarni S. R., 2007, ApJ, 660, 587

[13] Charles et al. (2008) incorrectly attribute UW CrB's superorbital period to 4U 1916−053.

Camilo F., Lorimer D. R., Freire P., Lyne A. G., Manchester R. N., 2000, ApJ, 535, 975
Campana S., Colpi M., Mereghetti S., Stella L., Tavani M., 1998, A&AR, 8, 279
Carney B. W., 1996, PASP, 108, 900
Casares J., Charles P. A., Naylor T., 1992, Nature, 355, 614
Charles P., Clarkson W., Cornelisse R., Shih C., 2008, New Astron. Rev., 51, 768
Chomiuk L., Strader J., Maccarone T. J., Miller-Jones J. C. A., Heinke C., Noyola E., Seth A. C., Ransom S., 2013, ApJ, 777, 69
Connolly S., 2015, preprint (arXiv:1503.06676)
Coppejans D. L., Körding E. G., Knigge C., Pretorius M. L., Woudt P. A., Groot P. J., Van Eck C. L., Drake A. J., 2016, MNRAS, 456, 4441
Davies M. B., Hansen B. M. S., 1998, MNRAS, 301, 15
de Martino D. et al., 2010, A&A, 515, A25
de Martino D. et al., 2013, A&A, 550, A89
de Martino D. et al., 2015, MNRAS, 454, 2190
Deller A. T. et al., 2015, ApJ, 809, 13
Deloye C. J., Bildsten L., 2003, ApJ, 598, 1217
Edmonds P. D., Gilliland R. L., Heinke C. O., Grindlay J. E., 2003a, ApJ, 596, 1177
Edmonds P. D., Gilliland R. L., Heinke C. O., Grindlay J. E., 2003b, ApJ, 596, 1197
Evans P. A., Beardmore A. P., Osborne J. P., Wynn G. A., 2009, MNRAS, 399, 1167
Fabian A. C., Pringle J. E., Rees M. J., 1975, MNRAS, 172, 15 plbibsc-p
Fender R. P., Gallo E., Jonker P. G., 2003, MNRAS, 343, L99
Foight D. R., Güver T., Özel F., Slane P. O., 2016, ApJ, 826, 66
Frank J., King A. R., Lasota J.-P., 1987, A&A, 178, 137
Freire P. C., Camilo F., Kramer M., Lorimer D. R., Lyne A. G., Manchester R. N., D'Amico N., 2003, MNRAS, 340, 1359
Fruscione A. et al., 2006, in Silva D. R., Doxsey R. E., eds, Proc. SPIE Conf. Ser. Vol. 6270, Observatory Operations: Strategies, Processes, and Systems. SPIE, Bellingham, p. 62701V
Furst F. et al., 2016, ApJ, 831, L14
Gallo E., Fender R. P., Pooley G. G., 2003, MNRAS, 344, 60
Gallo E., Migliari S., Markoff S., Tomsick J. A., Bailyn C. D., Berta S., Fender R., Miller-Jones J. C. A., 2007, ApJ, 670, 600
Gallo E. et al., 2014, MNRAS, 445, 290
García J., Kallman T. R., 2010, ApJ, 718, 695
García J., Kallman T. R., Mushotzky R. F., 2011, ApJ, 731, 131
García J., Dauser T., Reynolds C. S., Kallman T. R., McClintock J. E., Wilms J., Eikmann W., 2013, ApJ, 768, 146
Gehrels N., 1986, ApJ, 303, 336
Grindlay J. E., Hertz P., Steiner J. E., Murray S. S., Lightman A. P., 1984, ApJ, 282, L13
Grindlay J. E., Heinke C., Edmonds P. D., Murray S. S., 2001, Science, 292, 2290
Hakala P., Hjalmarsdotter L., Hannikainen D. C., Muhli P., 2009, MNRAS, 394, 892
Harrison F. A. et al., 2013, ApJ, 770, 103
Heinke C. O., Grindlay J. E., Lloyd D. A., Edmonds P. D., 2003a, ApJ, 588, 452
Heinke C. O., Grindlay J. E., Lugger P. M., Cohn H. N., Edmonds P. D., Lloyd D. A., Cool A. M., 2003b, ApJ, 598, 501
Heinke C. O., Grindlay J. E., Edmonds P. D., 2005a, ApJ, 622, 556
Heinke C. O., Grindlay J. E., Edmonds P. D., Cohn H. N., Lugger P. M., Camilo F., Bogdanov S., Freire P. C., 2005b, ApJ, 625, 796
Heinke C. O., Rybicki G. B., Narayan R., Grindlay J. E., 2006, ApJ, 644, 1090
Hertz P., Grindlay J. E., 1983, ApJ, 275, 105
Hills J. G., 1976, MNRAS, 175, 1P
Howell S. B., 2001, PASJ, 53, 675
Hunter J. D., 2007, Comput. Sci. Eng., 9, 90
Hynes R. I. et al., 2004, ApJ, 611, L125
Israel G. L. et al., 2016, preprint (arXiv:1609.07375)
Israel G. L. et al., 2017, MNRAS, 466, L48
Ivanova N., Heinke C. O., Rasio F. A., Taam R. E., Belczynski K., Fregeau J., 2006, MNRAS, 372, 1043
Ivanova N., Heinke C. O., Rasio F. A., Belczynski K., Fregeau J. M., 2008, MNRAS, 386, 553
Ivezić Ž., Connolly A., Vanderplas J., Gray A., 2014, Statistics, Data Mining and Machine Learning in Astronomy. Princeton Univ. Press, Princeton, NJ
Johnson T. J. et al., 2015, ApJ, 806, 91
Jonker P. G., Wijnands R., van der Klis M., 2004, MNRAS, 349, 94
Jordán A. et al., 2004, ApJ, 613, 279
Kallman T., Bautista M., 2001, ApJS, 133, 221
Katz J. I., 1975, Nature, 253, 698
Kimmig B., Seth A., Ivans I. I., Strader J., Caldwell N., Anderton T., Gregersen D., 2015, AJ, 149, 53
Knigge C., 2006, MNRAS, 373, 484
Knigge C., Zurek D. R., Shara M. M., Long K. S., 2002, ApJ, 579, 752
Knigge C., Zurek D. R., Shara M. M., Long K. S., Gilliland R. L., 2003, ApJ, 599, 1320
Knigge C., Dieball A., Maíz Apellániz J., Long K. S., Zurek D. R., Shara M. M., 2008, ApJ, 683, 1006
Koliopanos F., Gilfanov M., Bildsten L., 2013, MNRAS, 432, 1264
Kulkarni S. R., Hut P., McMillan S., 1993, Nature, 364, 421
Leahy D. A., Darbro W., Elsner R. F., Weisskopf M. C., Kahn S., Sutherland P. G., Grindlay J. E., 1983, ApJ, 266, 160
Linares M. et al., 2014, MNRAS, 438, 251
Lomb N. R., 1976, Ap&SS, 39, 447
Maccarone T. J., 2005, MNRAS, 360, L30
Maccarone T. J., Peacock M. B., 2011, MNRAS, 415, 1875
Maccarone T. J., Kundu A., Zepf S. E., Rhode K. L., 2007, Nature, 445, 183
McMullin J. P., Waters B., Schiebel D., Young W., Golap K., 2007, in Shaw R. A., Hill F., Bell D. J., eds, ASP Conf. Ser. Vol. 376, Astronomical Data Analysis Software and Systems XVI. Astron. Soc. Pac., San Francisco, p. 127
Madej O. K., García J., Jonker P. G., Parker M. L., Ross R., Fabian A. C., Chenevez J., 2014, MNRAS, 442, 1157
Magdziarz P., Zdziarski A. A., 1995, MNRAS, 273, 837
Marshall H. L., Tennant A., Grant C. E., Hitchcock A. P., O'Dell S. L., Plucinsky P. P., 2004, in Flanagan K. A., Siegmund O. H. W., eds, Proc. SPIE Conf. Ser. Vol. 5165, X-Ray and Gamma-Ray Instrumentation for Astronomy XIII. SPIE, Bellingham, p. 497
Mason P. A., Robinson E. L., Gray C. L., Hynes R. I., 2008, ApJ, 685, 428
Mewe R., Gronenschild E. H. B. M., van den Oord G. H. J., 1985, A&AS, 62, 197
Mewe R., Lemen J. R., van den Oord G. H. J., 1986, A&AS, 65, 511
Middleditch J., 1976, PhD thesis, California Univ., Berkeley
Migliari S., Fender R. P., 2006, MNRAS, 366, 79
Miller-Jones J. C. A., Gallo E., Rupen M. P., Mioduszewski A. J., Brisken W., Fender R. P., Jonker P. G., Maccarone T. J., 2008, MNRAS, 388, 1751
Miller-Jones J. C. A. et al., 2015, MNRAS, 453, 3918
Mooley K. P. et al., 2017, MNRAS, 467, 31
Morscher M., Umbreit S., Farr W. M., Rasio F. A., 2013, ApJ, 763, L15
Morscher M., Pattabiraman B., Rodriguez C., Rasio F. A., Umbreit S., 2015, ApJ, 800, 9
Nelemans G., Jonker P. G., 2010, New Astron. Rev., 54, 87
Nelemans G., Jonker P. G., Marsh T. R., van der Klis M., 2004, MNRAS, 348, L7
Nelemans G., Jonker P. G., Steeghs D., 2006, MNRAS, 370, 255
Nelemans G., Yungelson L. R., van der Sluys M. V., Tout C. A., 2010, MNRAS, 401, 1347
Noble M. S., Ji L., Young A., Lee J. C., 2009, in Bohlender D. A., Durand D., Dowler P., eds, ASP Conf. Ser. Vol. 411, Astronomical Data Analysis Software and Systems XVIII. Astron. Soc. Pac., San Francisco, p. 301
Pan Z., Hobbs G., Li D., Ridolfi A., Wang P., Freire P., 2016, MNRAS, 459, L26
Papitto A. et al., 2013, Nature, 501, 517
Papitto A., de Martino D., Belloni T. M., Burgay M., Pellizzoni A., Possenti A., Torres D. F., 2015, MNRAS, 449, L26

Paresce F., de Marchi G., Ferraro F. R., 1992, Nature, 360, 46
Patterson J., Raymond J. C., 1985, ApJ, 292, 535
Patterson J. et al., 2005, PASP, 117, 1204
Peuten M., Zocchi A., Gieles M., Gualandris A., Hénault-Brunet V., 2016, MNRAS, 462, 2333
Plotkin R. M., Gallo E., Jonker P. G., 2013, ApJ, 773, 59
Plotkin R. M., Gallo E., Markoff S., Homan J., Jonker P. G., Miller-Jones J. C. A., Russell D. M., Drappeau S., 2015, MNRAS, 446, 4098
Plotkin R. M. et al., 2016, MNRAS, 456, 2707
Pooley D. et al., 2003, ApJ, 591, L131
Press W. H., 1978, Comments Astrophys., 7, 103
Pretorius M. L., Mukai K., 2014, MNRAS, 442, 2580
Ransom S. M., Eikenberry S. S., Middleditch J., 2002, AJ, 124, 1788
Ransom S. M., Cordes J. M., Eikenberry S. S., 2003, ApJ, 589, 911
Rappaport S., Ma C. P., Joss P. C., Nelson L. A., 1987, ApJ, 322, 842
Reig P., Papadakis I., Kylafis N. D., 2003, A&A, 398, 1103
Ridolfi A. et al., 2016, MNRAS, 462, 2918
Rodriguez C. L., Morscher M., Pattabiraman B., Chatterjee S., Haster C.-J., Rasio F. A., 2015, Phys. Rev. Lett., 115, 051101
Rodriguez C. L., Haster C.-J., Chatterjee S., Kalogera V., Rasio F. A., 2016, ApJ, 824, L8
Russell T. D. et al., 2016, MNRAS, 460, 3720
Rutledge R. E., Bildsten L., Brown E. F., Pavlov G. G., Zavlin V. E., 1999, ApJ, 514, 945
Rutledge R. E., Bildsten L., Brown E. F., Pavlov G. G., Zavlin V. E., Ushomirsky G., 2002, ApJ, 580, 413
Salaris M., Weiss A., 1998, A&A, 335, 943
Salaris M., Held E. V., Ortolani S., Gullieuszik M., Momany Y., 2007, A&A, 476, 243
Sanna A. et al., 2017, A&A, 598, 34
Sault R. J., Teuben P. J., Wright M. C. H., 1995, in Shaw R. A., Payne H. E., Hayes J. J. E., eds, ASP Conf. Ser. Vol. 77, Astronomical Data Analysis Software and Systems IV. Astron. Soc. Pac., San Francisco, p. 433
Scargle J. D., 1982, ApJ, 263, 835
Sigurdsson S., Hernquist L., 1993, Nature, 364, 423
Sippel A. C., Hurley J. R., 2013, MNRAS, 430, L30
Stacey W. S., Heinke C. O., Elsner R. F., Edmonds P. D., Weisskopf M. C., Grindlay J. E., 2011, ApJ, 732, 46
Stappers B. W. et al., 2014, ApJ, 790, 39
Strader J., Chomiuk L., Maccarone T. J., Miller-Jones J. C. A., Seth A. C., 2012, Nature, 490, 71
Sutantyo W., 1975, A&A, 44, 227
Tendulkar S. P. et al., 2014, ApJ, 791, 77
Tetarenko B. E. et al., 2016, ApJ, 825, 10
Timmer J., Koenig M., 1995, A&A, 300, 707
Titarchuk L., 1994, ApJ, 434, 570
van Haaften L. M., Nelemans G., Voss R., Wood M. A., Kuijpers J., 2012, A&A, 537, A104
van Zyl L., Charles P. A., Arribas S., Naylor T., Mediavilla E., Hellier C., 2004, MNRAS, 350, 649
Vanderplas J., 2015, gatspy: General tools for Astronomical Time Series in Python. Available at: https://doi.org/10.5281/zenodo.14833
Vanderplas J., Connolly A., Ivezić Ž., Gray A., 2012, in Das K., Chawla N. V., Srivastava A. N., eds, Proc. Conference on Intelligent Data Understanding (CIDU), Introduction to astroML: Machine learning for astrophysics. p. 47. Available at: http://ieeexplore.ieee.org/xpl/mostRecentIssue.jsp?punumber=6373897
Vaughan B. A. et al., 1994, ApJ, 435, 362
Vaughan S., Uttley P., Markowitz A. G., Huppenkothen D., Middleton M. J., Alston W. N., Scargle J. D., Farr W. M., 2016, MNRAS, 461, 3145
Verbunt F., Hasinger G., 1998, A&A, 336, 895
Verbunt F., Hut P., 1987, in Helfand D. J., Huang J.-H., eds, Proc. IAU Symp. 125, The Origin and Evolution of Neutron Stars. Reidel, Dordrecht, p. 187
Verbunt F., Lewin W. H. G., 2006, in Lewin W. H. G., van der Klis M., eds, Compact Stellar X-ray Sources. Cambridge Univ. Press, Cambridge, p. 341
Verner D. A., Ferland G. J., Korista K. T., Yakovlev D. G., 1996, ApJ, 465, 487
Walter F. M., Mason K. O., Clarke J. T., Halpern J., Grindlay J. E., Bowyer S., Henry J. P., 1982, ApJ, 253, L67
White N. E., Angelini L., 2001, ApJ, 561, L101
White N. E., Holt S. S., 1982, ApJ, 257, 318
Wijnands R., van der Klis M., 1998, Nature, 394, 344
Wijnands R., Degenaar N., Armas Padilla M., Altamirano D., Cavecchi Y., Linares M., Bahramian A., Heinke C. O., 2015, MNRAS, 454, 1371
Wilms J., Allen A., McCray R., 2000, ApJ, 542, 914
Wilson W. E. et al., 2011, MNRAS, 416, 832
Woodley K. A. et al., 2012, AJ, 143, 50
Zechmeister M., Kürster M., 2009, A&A, 496, 577

This paper has been typeset from a TEX/LATEX file prepared by the author.